This article has been accepted for publication in IEEE Open Journal of the Industrial Electronics Society. This is the author's version which has not been fully edited and content may change prior to final publication. Citation information: DOI 10.1109/OJIES.2025.3559447

Date of publication xxxx 00, 0000, date of current version xxxx 00, 0000.
Digital Object Identifier XX.XXXX/YYY.20XX.ZZZZZZZ

Optimized Sigmoid-Based Complete Ensemble Empirical Mode Decomposition for Energy Management in Hybrid Electric Vehicles

LUCAS JONYS RIBEIRO SILVA[1], (Graduate Student Member, IEEE), MÁRCIO VON RONDOW CAMPOS[1], THALES AUGUSTO FAGUNDES[1], BRUNO MENEGHEL ZILLI[1], RODOLPHO VILELA ALVES NEVES[2], RICARDO QUADROS MACHADO[1], (Senior Member, IEEE), and VILMA ALVES DE OLIVEIRA[1], (Life Senior Member, IEEE)

[1]Sao Carlos School of Engineering, University of Sao Paulo, Sao Carlos SP 13566-590, Brazil
[2]Federal University of Viçosa, Viçosa MG 36570-900, Brazil

Corresponding author: Lucas Jonys Ribeiro Silva (e-mail: lucasjonys@usp.br).

This work was supported by the Coordination for the Improvement of Higher Education Personnel (CAPES) under grants PDSE-88881.187771/2018-01, 88881.030370/2013-0 and 88887.682783/2022-00, the National Council for Scientific and Technological Development (CNPq) under grant 309624/2018-5, the Research Development Foundation (FUNDEP) Rota 2030/Line V under grant 27192/27 and the Sao Paulo Research Foundation (FAPESP) under grants 2020/05865-3, 2022/00628-9 and 2024/00607-7.

ABSTRACT This paper proposes a sigmoid-based particle swarm optimization (PSO) for a complete ensemble empirical mode decomposition (SPSO-CEEMD) applied to the energy management system (EMS) of a hybrid electric vehicle (HEV). The low-frequency power demand, to be supplied by the lithium-ion battery (LIB) and internal combustion engine (ICE), is calculated by the CEEMD, while sigmoid functions define the ICE reference, avoiding discontinuities in the control strategy and limiting the response frequency in the implementation of power, velocity and angle control loops for the ICE butterfly valve actuator. High-frequency demand is handled by the ultracapacitor (UC), which controls the dc-link voltage. The sigmoid functions are optimized to reduce the ICE fuel consumption and the LIB aging, considering ICE emissions as constraints in the PSO. To make the UC available in next peak demands, its terminal voltage restoration is relaxed by a phase-lag compensator (PLC) tuned to actuate only after power delivers, which reduces the influence in the LIB dynamic. Experimental and numerical results under the HWYCOL, SC03 and a Brazilian real-world drive cycles show that SPSO-CEEMD reduces the total operational cost, LIB stress and aging compared to state-of-the-art strategies. Despite larger UC voltage restoration error with the PLC, LIB power dynamic is not significantly affected, increasing its lifetime by 2.74% and 10.96% compared to traditional PI and low-pass filter strategies, respectively. Moreover, the total operational cost is reduced by 18.28% and 47.54% in relation to the exclusive operation strategy (XOS) and interval type-2 fuzzy logic control (IT2-FLC) adapted from the literature.

INDEX TERMS Hybrid electric vehicle, sigmoid functions, energy management system, empirical mode decomposition, voltage restoration.

NOMENCLATURE

Abbreviations

ANN	artificial neural network
BBC	bidirectional boost converter
CEEMD	complete ensemble empirical mode decomposition
CO	carbon monoxide
NO_x	nitrous oxides
DoD	depth of discharge
EMD	empirical mode decomposition
EMS	energy management system
EoL	end-of-life
FC	fuel cell
FLC	fuzzy logic controller
GA	genetic algorithm
HEV	hybrid electric vehicle
HIL	hardware-in-the-loop

This article has been accepted for publication in IEEE Open Journal of the Industrial Electronics Society. This is the author's version which has not been fully edited and content may change prior to final publication. Citation information: DOI 10.1109/OJIES.2025.3559447

HPTS	hysteresis power threshold strategy
ICE	internal combustion engine
ICEV	internal combustion engine vehicle
IMF	intrinsic mode function
IT2	interval type-2
LIB	lithium-ion battery
LBS	learning-based strategy
LPF	low-pass filter
LUT	lookup table
OBS	optimization-based strategy
PBC	passivity-based control
PE	permutation entropy
PEV	pure electric vehicle
PI	proportional-integral
PLC	phase-lag compensator
PMSM	permanent magnetic synchronous machine
PFCS	power follower control strategy
P-HEV	parallel hybrid electric vehicle
PMP	Pontryagins minimum principle
PWM	pulse-width modulation
PSO	particle swarm optimization
RBS	rule-based strategy
RL	reinforcement learning
S-HEV	series hybrid electric vehicle
SoC	state-of-charge
SoH	state-of-health
SSS	start-stop system
TCS	thermostat control strategy
UC	ultracapacitor
WT	Wavelet transform
XOS	exclusive operation strategy

Variables and constants

v_b, i_b	LIB voltage and current
E_a	LIB activation energy
z, c	LIB power-law factor and c-rate
Ah	total Ampere-hour throughput
v_{oc}	LIB open circuit voltage
C_b, E_b	LIB capacity and energy
Λ	LIB pre-exponential factor
SoC_b	LIB SoC
DoD_b	LIB DoD
$\mathrm{SoC}_{\min}$	LIB minimum SoC
$\mathrm{SoC}_{\max}$	LIB maximum SoC
SoH_b	LIB SoH
$\mathrm{SoH}_b^{\mathrm{end}}$	LIB final SoH
β_{LIB}	LIB pack price
v_u, i_u	UC voltage and current
Δv_{uc}	UC restoration control input
i_{uc}^*, v_{uc}^*	UC reference current and reference voltage
F_t	traction force
M_v, A_v	vehicle total mass and front area
g	gravitational acceleration
R	ideal gas constant
v_x, $\overline{v}_x$	vehicle speed and average speed
c_r, c_κ	rolling resistance and slip stiffness
f_F, k_R	friction coefficient and tire slip
ρ_a, ρ_f	air and fuel density
C_d	aerodynamic coefficient
P_d	instantaneous power demand
$\mathcal{P}[n]$	HEV power demand sequence
ω_h, $\mathcal{T}_h$	high-speed shaft angular velocity and torque
ω_l, $\mathcal{T}_l$	low-speed shaft angular velocity and torque
K_{sh}, B_{sh}	high-speed shaft stiffness and damping
K_{sl}, B_{sl}	low-speed shaft stiffness and damping
N_{rdl}, N_{rdh}	low-speed and high-speed shafts output speed
r_d	wheel radius
r_L	load tire radio
J_r, η_r	speed reducer inertia and efficiency
J_m	traction motor inertia
B_m	traction motor viscous friction coefficient
P_e, η_e	ICE power and efficiency
$\dot{m}_f$	ICE fuel consumption
$P_e^{\max}$	ICE maximum power
b_e	ICE fuel consumption rate
γ_μ	ICE power coefficients
P_g, η_g	generator power and efficiency
ω_e, $\mathcal{T}_e$	ICE angular velocity and torque
ω_g, $\mathcal{T}_g$	generator angular velocity and torque
ω_n	ICE normalized angular velocity
P_o	ICE low-rotation reference power
ω_{pp}	angular velocity for maximum power
θ, τ_v	butterfly valve angle and delay
J_e, J_g	ICE and generator inertia
T_f	ambient temperature
T_c, T_s	LIB core and surface temperature
T_a, T_a^{end}	LIB internal temperature and its final value
$\mathcal{S}_{\mathrm{low}}$, $\mathcal{S}_{\mathrm{high}}$	low and high demand sigmoid functions
κ	sigmoid steepness
α	power sharing coefficient
$c_1, c_2,$	PSO acceleration coefficients
N_p	PSO number of particles
Cost	total operational cost
Υ_m, Υ_s	PSO weights
P_{LF}	low-frequency power demand
$P_{b\mathrm{ICE}}^*$	LIB and ICE reference power
P_{ICE}^*	ICE reference power
$P_{\mathrm{ICE}}^{\max}$	ICE maximum power
P_b^*	LIB reference power
w^h, τ	white noise and PE time delay
K_m, K_c	dc motor and chopper PWM gains
m, v	PE embedding dimension and vector
ξ	normalized PE
$P_o^{\mathrm{A}}, P_o^{\mathrm{B}}$	control parameters
L_d, ϕ	road distance and slope
A_w, D_w	low and high-frequency wavelet components
σ_w	high-frequency component standard deviation
β_f, β_b	fuel cost and LIB energy cost
IMF_k, r_k	k-th IMF and its residue

I. INTRODUCTION

THE automotive industry has long faced challenges related to environmental pollution, primarily due to greenhouse gas emissions from internal combustion engine vehicles (ICEVs) and a heavy reliance on a singular energy source. The reduction of gas emissions has been extensively addressed in both academic research and legislative frameworks [1]. In response, the adoption of electric vehicles (EVs) and hybrid electric vehicles (HEVs) has gained widespread acceptance as potential solutions [2]–[4]. Among these, HEVs have emerged as the most widely adopted option, offering superior fuel efficiency compared to traditional ICEVs, while providing a longer cruising range than purely electric vehicles (PEVs) [5]. Moreover, the main pollutants as carbon monoxide (CO) and nitrous oxides (NO_x) can be reduced [6].

To accommodate varying load dynamics, the powertrain architecture of HEVs has become increasingly diversified [2]. Ultracapacitors (UCs), with their high power density and extended life cycle, are utilized to supply and absorb high-frequency power demands. In contrast, low-frequency power demands are managed by other energy sources, such as batteries and internal combustion engines (ICEs) [3], [4]. Although the combination of a battery and UC as a hybrid storage system can enhance the HEV powertrain by integrating high specific energy storage with high specific power storage [3], many studies have not adopted this configuration. Even though UC control requires an additional dc-dc converter, its implementation enables each energy source to operate according to its dynamic response, thereby contributing to improve efficiency [4], [7]. However, managing multiple energy sources efficiently poses significant challenges, particularly concerning battery longevity and overall system performance.

For lithium-ion batteries (LIBs), one of the key performance indicators is the state-of-health (SoH), which is defined as the ratio between the current and initial capacity [8]. This metric is closely linked to LIB aging and its eventual end-of-life (EoL). Given that the battery is among the most expensive components of an EV [9], it is essential to monitor and control factors that contribute to its aging, such as temperature, charge and discharge currents, and depth-of-discharge (DoD) [9], [10]. Given these challenges, effective management of HEV energy sources is crucial. To this end, various EMS strategies have been proposed, which can be broadly classified into rule-based strategies (RBSs), optimization-based strategies (OBSs), and learning-based strategies (LBSs) [11], [12].

Due to their simplicity, low implementation complexity and ideal real-time performance [13], [14], various RBSs have been proposed in the literature. To reduce energy consumption, Phan et al. [15] introduced an interval type-2 fuzzy logic controller (IT2-FLC) to manage the uncertainties of driving conditions within an intelligent EMS for parallel hybrid electric vehicles (P-HEVs). While this approach yields a higher final state-of-charge (SoC) and improved energy efficiency compared to traditional fuzzy logic controllers (FLCs), it does not account for battery SoH or thermal effects. Building on the thermostat control strategy (TCS) and power follower control strategy (PFCS), Shabbir and Evangelou's exclusive operation strategy (XOS) [16] enhanced the optimality of RBSs [17]. However, the number of ICE restarts in the ON-OFF operation mode is high, which can increase the pollutant emissions [18]. This is due to the fact that the emissions are reduced when the engine catalyst temperature reaches the light-off temperature [19], which is affected by start-stop system (SSSs). Furthermore, frequent engine restarts may generate noticeable noise and vibrations, potentially compromising passenger comfort.

Due to the limitations pointed out in the above mentioned approaches, alternative strategies incorporating neural network and signal processing techniques have been explored. Benmouna et al. [20] utilized an artificial neural network (ANN) in combination with passivity-based control (PBC) within the EMS. The ANN determines the battery reference current, while the PBC ensures compliance with this reference. Although this approach reduces battery stress, it leads to nearly constant current, suggesting underutilization of the energy source. Moreover, SoH is not included into this strategy, and the optimization of operating points for the energy sources is not addressed. Numerous other studies have employed WT to separate high and low-frequency power demands [21]–[23]. Nonetheless, the effectiveness of this method is strongly influenced by the choice of the base wavelet function and the number of decomposition levels [3].

Despite their low computational complexity and robust real-time performance, RBSs rely heavily on expert knowledge [14], [24]. Moreover, optimal results for fuel economy are not achieved [13]. To improve the RBSs performance, several works have combining them with OBSs. An optimized frequency decoupling strategy that combines a FLC with Wavelet transform (WT) is employed in [25], [26]. In this approach, the FLC determines the cut-off frequency of a low-pass filter (LPF), which is used to compute the UC reference, while WT handles power allocation based on the power demand frequency. However, the use of an LPF still permits some high-frequency demand to be achieved by the battery and the SoH is not considered. Additionally, the SoC reference for the UC is dependent on the vehicles speed. An optimized hysteresis power threshold strategy (HPTS) with an energy-based SSS for fuel optimization, including a fuel penalty for engine starts, was presented in [17]. The power reference for each source is defined according a 2-D map constructed according to an optimum analytical solution. To avoid excessive ICE state transitions, an hysteresis switching scheme is adopted. Moreover, Campos et al. [4] combined a RBS with offline optimization to reduce both fuel consumption and battery usage. However, battery aging and pollutant

This article has been accepted for publication in IEEE Open Journal of the Industrial Electronics Society. This is the author's version which has not been fully edited and content may change prior to final publication. Citation information: DOI 10.1109/OJIES.2025.3559447

emissions were not considered in [4], [17].

Numerous works have employed LBSs in the EMS of HEVs. Tang et al. [13] proposed a strategy based on deep reinforcement learning (RL) combined with a rule-based SSS to enhance fuel efficiency. However, pollutant emissions, which are significantly influenced by the SSS, were neglected. Similarly, Wang et al. [24] proposed the merging of Bayesian optimization with deep RL to improve robustness and reduce dependence on real-world data. Although energy consumption is reduced by the strategy, battery thermal model and aging were not considered, nor does it account for ICE emissions or actuator dynamics. A data driven RL method is proposed in [14] to the EMS in a HEV to improve the learning from a static offline dataset and the fine-tuning process while minimizes the fuel consumption. Battery aging, ICE emissions an actuator were overlooked. As highlighted by Hong et al. [19], most studies focusing on fuel consumption minimization tend to result in increased harmful gas emissions, demonstrating a typical trade-off between fuel savings and emissions.

Despite the optimal performance, LBSs require a large training data [4], [12]. These strategies are commonly used in autonomous vehicles, but still suffer with low reliability and safety in this application [27]. On the other hand, online OBSs application faces the problem of requiring high computational effort and memory [4], which makes their application in the onboard computation units of HEVs unfeasible [17]. For these reasons, RBSs are more commonly used in commercial HEVs [4], [17].

Although the recent strategies have made significant progress in optimizing the utilization of energy sources, the negative impact of high-frequency demands on battery performance is frequently neglected. To allocate high and low-frequency demands among the sources without the need for predefined basis functions, as required in Wavelet and Fourier-based strategies, the empirical mode decomposition (EMD) technique has emerged as a promising alternative [3]. The original signal is adaptively decomposed by EMD based on its temporal characteristics.

A challenge of the EMD techniques is that discontinuous signals may be improperly decomposed due to modal aliasing [28]. This issue can be addressed using the complete ensemble empirical mode decomposition (CEEMD) strategy [29]. Shen et al. [3] applied the CEEMD combined with permutation entropy (PE) to reduce high-frequency demands on the battery in EVs. Nevertheless, this approach requires adaptation for HEVs. Although battery aging is mitigated, the strategy does not achieve an optimal operating point for each energy source and a detailed battery thermal model is not developed, which can affect the accuracy of SoH evaluation.

Considering the crucial role of the battery in EMSs, a pre-heating strategy is proposed in [30] for a P-HEV. The battery pre-heating time is defined by a particle swarm optimization (PSO) problem, while the EMS is governed by using the Pontryagin's minimum principle (PMP) to reduce fuel consumption and battery aging. However, the ICE emissions and actuator were neglected. Zha et al. [12] developed a time-efficient battery temperature sensitive EMS for a S-HEV. The strategy reduces the fuel consumption and keeps the battery temperature in the thermal comfort zone. Nonetheless, the ICE emissions and actuator were not taken into account, and the battery aging was not directly considered.

While temperature management is crucial for optimizing battery performance, another significant factor impacting the system's efficiency is the performance of the UC. After the device delivers power during high-frequency transients, its terminal voltage drops, which may limit its ability to manage subsequent charging and discharging cycles [3]. Therefore, restoring the UC voltage is critical, and various strategies have been proposed in the literature. Bastos et al. [31] introduced a method where the output of a LPF is added to the current reference of the device. The time constant is tuned to delay voltage restoration relative to current peaks by narrowing the voltage restoration bandwidth. In [32], a proportional-integral (PI) controller processes the UC terminal voltage error, generating an additional term that is split between the battery and UC in a microgrid, though no specific design criteria for the controller were provided. In Shen et al. [3], a method based on FLC to maintain the UC SoC at an appropriate level is proposed. However, the development of FLC strategies relies on expert knowledge.

Regarding the ICE in HEV, the use of discontinuous strategies to manage the ICE can be prejudicial. For instance, when the ICE shifts between two operating points with a considerable power difference, the resulting discontinuity can cause undesirable high-frequency oscillations. Additionally, the butterfly valve may not respond effectively due to its slower dynamic characteristics, making necessary to use a faster valve, which can increase the costs. In this way, although sigmoid functions have been widely utilized in various fields, such as SoC equalization [33] and dc microgrid control [34], their application in ICE management has not been thoroughly explored. These nonlinear functions offer several advantages, including a reduced number of tuning parameters, adaptability to diverse operational conditions, and continuity, making them strong candidates for ICE management.

Despite the importance of considering the actuator dynamics, many authors neglect them in the management and control, focusing only on the power balance equation [2], [5], [12], [16], [17], [35]. However, in practical applications, neglecting actuator dynamics can significantly impact stability and performance, as time delays and mechanical characteristics can alter system behavior. To address such challenges in valve control, a dual-loop cascade control strategy is proposed in [36] for a P-HEV. The outer loop regulates the longitudinal speed of the P-HEV, setting the torque reference to be supplied by the engines. The torque reference for the electric motor is used in a lookup table (LUT) to determine the reference angle, which is then em-

TABLE 1. State-of-art works and proposed strategy: features comparison

Reference	Features (i)	(ii)	(iii)	(iv)	(v)	(vi)
This paper	✓	✓	✓	✓	✓	✓
[2], [13]	×	✓	×	×	×	×
[3], [21], [23]	×	×	*	✓	*	✓
[25]	×	×	*	✓	*	×
[4]	×	✓	×	✓	×	✓
[17]	×	✓	×	✓	×	×
[5]	✓	✓	×	×	×	✓
[35]	✓	✓	×	×	×	×
[15], [16]	×	×	×	✓	×	×
[26]	×	✓	*	✓	*	✓
[20]	×	✓	*	×	*	✓
[30]	✓	✓	×	✓	×	×
[38]	✓	✓	*	×	*	×
[12]	✓	✓	×	✓	×	×
[14], [24]	×	✓	×	×	×	×

*Not applicable. Powertrain using fuel cell or other sources instead of ICE.

ployed in an outer angle control loop. However, LUT-based methods have the disadvantage of relying on predefined conditions established by pre-constructed maps [37], which do not account for real-time variations or uncertainties in engine behavior.

The above literature review highlighted the key attributes of each proposal with respect to the features: (i) inclusion of battery thermal effects and aging model in the EMS; (ii) optimization of fuel consumption and/or LIB aging; (iii) consideration of ICE emissions in the management/optimization; (iv) low computational complexity and no need for training data; (v) incorporation of the dynamic of the ICE actuator in both EMS and control, and (vi) integration of the battery and UC in a fully active topology, wherein both sources are controllable via a dc-dc converters. The comparison in relation to the literature state-of-art works is exhibited in Table 1.

This paper proposes a combined approach using CEEMD, PE and sigmoid functions to address battery aging, fuel consumption and ICE emissions in a S-HEV. For the best of authors' knowledge, this is the first application of the CEEMD and PE approach in the EMS of a HEV. The main contributions are summarized as follows:

1) Effectively mitigates high-frequency demands on the LIB and ICE without requiring basis functions, as needed in traditional WT strategies;
2) Avoid discontinuities that could cause high-frequency oscillations, and accommodates the slow dynamics of the ICE butterfly valve actuator by using sigmoid functions in the ICE management and a triple control loop strategy;
3) Ensures that UC voltage restoration occurs after the power peaks, minimizing any significant impact on the dynamic response of the other energy sources;
4) Balances the fuel consumption and LIB aging by optimizing the parameters of sigmoid functions and the demand distribution between the LIB and ICE while simultaneously consider the ICE emissions as constraints in a optimization problem.

The rest of this paper is organized as follows. Section II presents the HEV powertrain structure and sources modeling. In Section III, the proposed SPSO-CEEMD strategy is discussed. Later, in Section IV, numerical and experimental results are shown, while the conclusion and future works are in Section V.

Notation: The sets $\mathbb{N}$, $\mathbb{R}_+$ and $\mathbb{R}_+^*$ denotes the set of natural, non negative real and strictly positive real numbers respectively, and $\operatorname{sign}(x) = x/|x| \quad \forall x \neq 0$.

II. POWERTRAIN STRUCTURE AND MODELING

The series HEV (S-HEV) powertrain consists of a LIB, an UC, and an ICE coupled to a generator. Both the LIB and UC are connected to the dc-link via bidirectional boost converters (BBCs), controlled by pulse-width modulation (PWM) with duty-cycles d_b and d_{uc}, respectively, as shown in Fig. 1. The pulses p_b and $\overline{p}_\mathrm{b}$, as well as p_uc and $\overline{p}_\mathrm{uc}$, are complementary.

A. VEHICULAR DYNAMIC

1) Longitudinal dynamics

Considering the HEV energy consumption, the longitudinal dynamic is used to calculate the traction force as [30]:

$$F_t = M_v\left[\dot{v}_x + c_r g\cos(\phi) + g\sin(\phi)\right] + \tfrac{1}{2}\rho_a C_d A_v v_x^2 \tag{1}$$

where M_v is the vehicle total mass, C_d is the aerodynamic drag coefficient, A_v is the front area, ρ_a is the air density, ϕ is the road slope, v_x is the longitudinal velocity and c_r is the rolling resistance, calculated as [39]:

$$c_r = \frac{r_L}{r_d}c_\kappa k_R + f_F - c_\kappa k_R \tag{2}$$

where r_d is the wheel radio, r_L is the load tire radio, c_κ is the tire normalized longitudinal slip stiffness, f_F is the friction coefficient and k_R is the tire slip, given by [40]:

$$k_R = \frac{\omega_l r_L - v_x}{v_x} \tag{3}$$

where ω_l is the wheel angular velocity

Remark 1: Considering the free rolling tire model, the value of c_κ depends on k_R, which is neglected in this paper for simplification. Moreover, parasitic forces such as toe and camber, temperature, water and pressure effects are also neglected. All these influences can be analyzed in [40].

2) Transmission unit

The transmission unit couples the electric motor, which operates at a high angular velocity ω_h, to the vehicle wheels, rotating at a lower angular velocity ω_l, through a gear reducer connecting the high-speed and low-speed shafts, as illustrated in Fig. 2a [41]. The dynamic models of both the high-speed and low-speed shafts from Matlab® were employed, with their respective torques computed as:

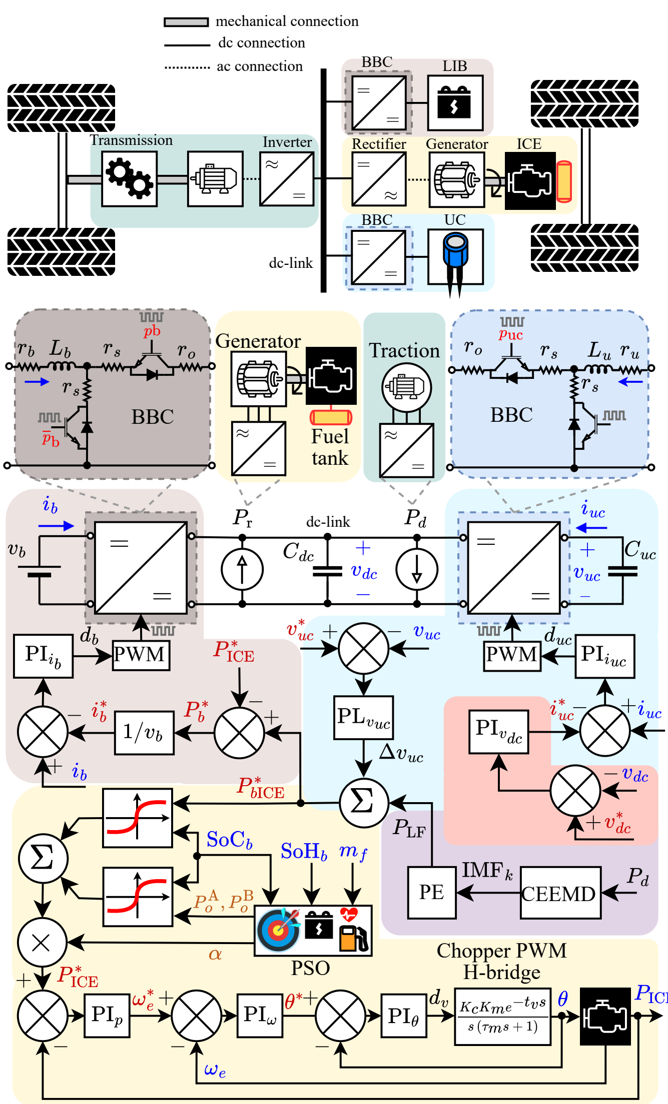

FIGURE 1. S-HEV powertrain and proposed SPSO-CEEMD EMS.

$$\dot{\mathcal{T}}_h = K_{sh}\left(\omega_h - N_{\text{rdh}}\right) + B_{sh}\left(\dot{\omega}_h - \dot{N}_{\text{rdh}}\right) \tag{4a}$$

$$\dot{\mathcal{T}}_l = K_{sl}\left(N_{\text{rdl}} - \omega_l\right) + B_{sl}\left(\dot{N}_{\text{rdl}} - \dot{\omega}_l\right) \tag{4b}$$

where N_{rdh} and N_{rdl} denote the output speeds of the high-speed and low-speed sides, respectively, while K_{sh} and B_{sh} represent the stiffness and damping of the high-speed shaft, and K_{sl} and B_{sl} correspond to the stiffness and damping of the low-speed shaft. The speed reducer is modeled according to [41]:

$$J_r\dot{N}_{\text{rdh}} = \mathcal{T}_h - i_r^{-1}\eta_r^{\text{sign}(\mathcal{T}_{\text{h}})}\mathcal{T}_l \tag{5}$$

with J_r and η_r representing the speed reducer inertia and efficiency, respectively, $i_r \triangleq N_{\text{rdh}}/N_{\text{rdl}}$ corresponding to the reduction ratio [42], and $\mathcal{T}_l$ is the low-speed shaft torque.

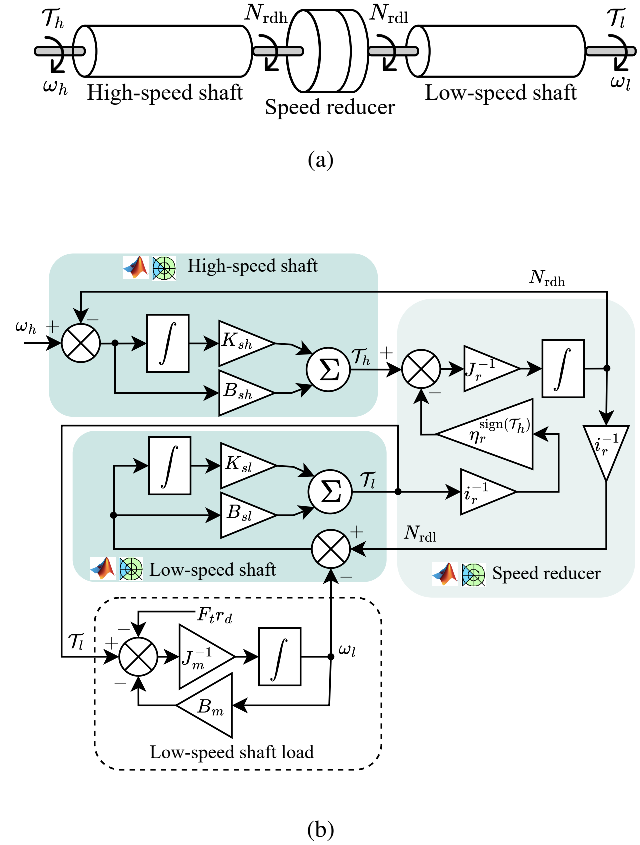

FIGURE 2. HEV transmission unit: (a) Mechanical schematic [41] and (b) block diagram modeling.

The load coupled to the low-speed shaft is related to wheels inertia, mechanical resistances and the viscous friction coefficient of the motor, being calculated as [41], [42]:

$$J_m\dot{\omega}_l = \mathcal{T}_l - F_t r_d - B_m\omega_l \tag{6}$$

where J_m is inertia of the vehicle's wheels concentrated on the rotor axis, r_d is the wheel radius, and B_m is the viscous friction coefficient of the motor. Therefore, the instantaneous power demand can be calculated as $P_d = \mathcal{T}_h\omega_h$. The block diagram for the complete unit transmission is shown in Fig. 2b.

Remark 2: The electric motor traction control is not the focus of this work. Therefore, it is considered that the HEV reaches the desired velocity throughout the operation. Although machine control is not implemented in this work, it is widely studied in the literature and its application for a permanent magnetic synchronous machine (PMSM) can be seen in [41], [42].

B. LITHIUM-ION BATTERY

The LIB model is crucial for representing its nonlinearities, which can influence the EMS. The adopted equivalent circuit model is the first-order RC, as shown in Fig. 3a. By applying

This article has been accepted for publication in IEEE Open Journal of the Industrial Electronics Society. This is the author's version which has not been fully edited and content may change prior to final publication. Citation information: DOI 10.1109/OJIES.2025.3559447

Kirchhoffs laws, the electrical model is defined as:

$$v_b = v_{oc} - R_{ob} i_b - v_{RC} \tag{7a}$$

$$\dot{v}_{RC} = \left(C_1 R_1\right)^{-1} \left(R_1 i_b - v_{RC}\right) \tag{7b}$$

where R_{ob} is the ohmic resistance, R_1 and C_1 are the polarization resistance and polarization capacitor, i_b and v_b are the LIB current and voltage, respectively, while v_{RC} is the terminal voltage on the RC circuit. The LIB resistances are higher for extremes SoC, as shown in Fig. 4. Therefore, it is recommended maintain SoC_b within a certain level [43], once operating the LIB at extreme SoCs reduce its lifetime [33], [34]. The relationship between open-circuit voltage v_{oc} and SoC (estimated by the Coulomb's counting method) is given by the function $f : \mathbb{R}_+ \to \mathbb{R}_+^*$, shown in Fig. 5a.

1) Aging model:

The LIB aging is related to its excessive usage, reaching a large number of cycles, which leads to a reduction of the capacity until reach the EoL [30]. This behavior can be measured by the SoH, calculated as [5]:

$$\dot{\mathrm{SoH}}_b = -\frac{|i_b|}{2 N_b C_b} \tag{8}$$

where N_b is the number of cycles and C_b is the LIB capacity. When the remaining available capacity reaches 20% of the nominal value, the EoL is reached and the total Ampere-hour A_h throughput can be calculated according to the Arrhenius' equation as [5]:

$$A_h = \left[\frac{20}{\Lambda \exp^{(E_a/\mathrm{R}T_a)}}\right]^{1/z} \tag{9a}$$

$$E_a = 310.3c - 31,700 \tag{9b}$$

where R is the ideal gas constant, E_a is the activation energy, T_a is the LIB average temperature, z is the power-law factor and Λ is the pre-exponential factor, that depends on the LIB c-rate according to function $g : \mathbb{R}_+ \to \mathbb{R}_+^*$ (see Fig. 5b). Therefore, the number of cycles N_b is given by [5], [30]:

$$N_b = 3,600 A_h / C_b \tag{10}$$

which allows evaluate the SoH in (8). As can be seen in (9a), the aging model is dependent on the temperature T_a, which requires a thermal model development.

2) Thermal model:

Considering an longitudinal homogeneous cylindrical LIB, as shown in Fig. 3b [35], the energy conservation principle produces the thermal state-space model [38]:

$$\begin{bmatrix} \dot{T}_s \\ \dot{T}_c \end{bmatrix} = \begin{bmatrix} \frac{-(R_c+R_u)}{R_u R_c C_s} & \frac{1}{R_c C_s} \\ \frac{1}{R_c C_c} & \frac{-1}{R_c C_c} \end{bmatrix} \begin{bmatrix} T_s \\ T_c \end{bmatrix} + \begin{bmatrix} \frac{1}{R_u C_s} & 0 \\ 0 & \frac{1}{C_c} \end{bmatrix} \begin{bmatrix} T_f \\ Q \end{bmatrix} \tag{11}$$

where T_s, T_c and T_f are the LIB surface, core and ambient temperature, respectively, R_c and R_u are resistances that represent the heat conduction inside and at the surface, while C_c and C_s are the core and surface heat capacities. The internal temperature is given by $T_a = 0.5\left(T_c + T_s\right)$ [35], [38], while the heat generation rate Q is calculated as:

$$Q = i_b \left(v_b - v_{oc}\left(\mathrm{SoC}_b\right)\right) + i_b T_c \frac{\partial v_{oc}\left(\mathrm{SoC}_b\right)}{\partial T_c}. \tag{12}$$

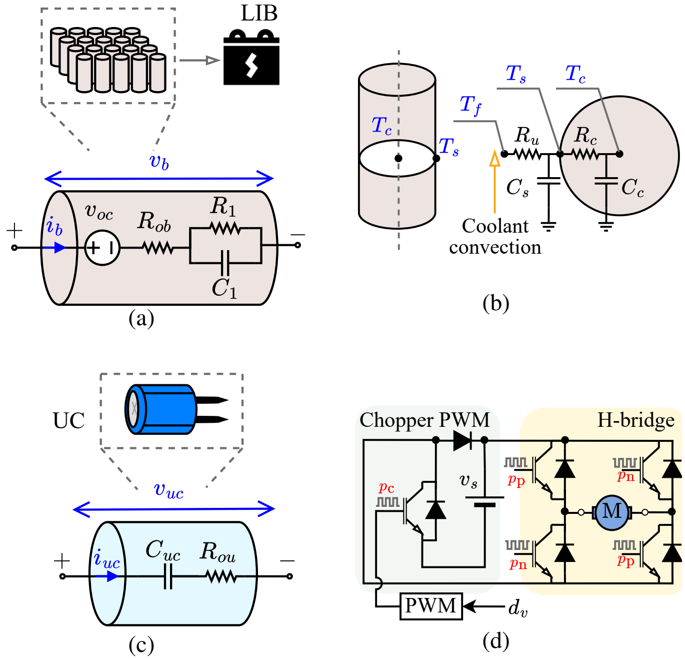

FIGURE 3. Sources modeling: (a) LIB electrical model, (b) LIB thermal model, (c) UC, and (d) ICE butterfly valve actuator.

C. ULTRACAPACITOR

To precisely modeling the UC without a large computational cost, the equivalent circuit of an ideal capacitor C_{uc} with a series resistance R_{ou} was applied, shown in Fig. 3c, due to its simplicity. The UC SoC is proportional to its terminal voltage v_{uc} [3].

D. INTERNAL COMBUSTION ENGINE AND GENERATOR

The ICE actuator, shown in Fig. 3d, consists of a dc source v_s modulated by an H-bridge according the duty-cycle d_v. The H-bridge command the dc motor (M) rotation by the complementary pulses p_p and p_n, while the ICE dynamic is modeled by the third order polynomial approximation pre-

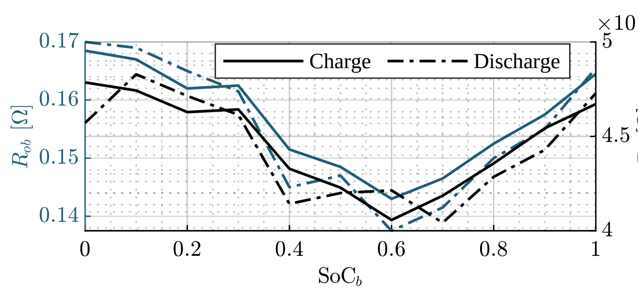

FIGURE 4. LIB resistances as a function of SoC.

This article has been accepted for publication in IEEE Open Journal of the Industrial Electronics Society. This is the author's version which has not been fully edited and content may change prior to final publication. Citation information: DOI 10.1109/OJIES.2025.3559447

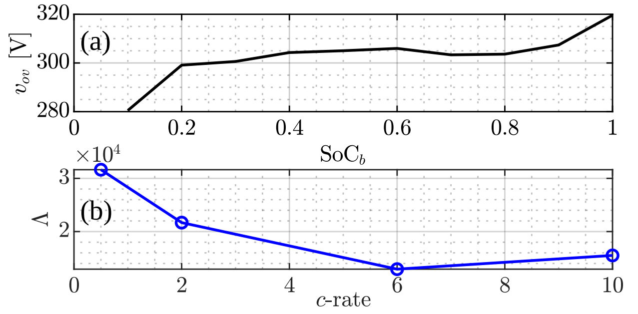

FIGURE 5. Battery modeling: (a) LIB open circuit voltage as a function of SoC and (b) Pre-exponential factor Λ as a function of c-rate [5].

sented in [44]. Therefore, the ICE power can be calculated as:

$$P_e = \frac{P_e^{\max}\theta}{100} \sum\nolimits_{\mu=1}^{3} \gamma_\mu \omega_n^\mu \tag{13}$$

where $\omega_n \triangleq \omega_e/\omega_{pp}$ with ω_e the ICE angular velocity and ω_{pp} the angular velocity for maximum power $P_e^{\max}$, $\gamma_\mu \in \mathbb{R}$ are coefficients dependent on the ICE used, with $\mu \in \{1,2,3\}$, and $\theta \in [0 \ \ 100\%]$ is the butterfly valve angle. Moreover, the coupling between the ICE and generator is modeled by the rotational relationship [5]:

$$\left(r_{eg}^{-2} J_e + J_g\right) \dot{\omega}_g = \mathcal{T}_e r_{eg}^{-1} - \mathcal{T}_g \tag{14}$$

where J_e and J_g are the ICE and generator inertia, ω_g is the generator angular velocity, $\mathcal{T}_e$ and $\mathcal{T}_g$ are the ICE and generator torque, respectively, and $r_{eg} \triangleq \omega_g/\omega_e$. The generator power P_g and the rectifier power P_r are given by:

$$P_g = \mathcal{T}_g \omega_g \eta_g \tag{15a}$$
$$P_r = P_g \eta_r \tag{15b}$$

where η_g and η_r are the generator and rectifier efficiencies, respectively.

1) ICE fuel consumption map

The ICE fuel consumption is calculated by a quasi-static model as [2]:

$$\dot{m}_f = \frac{\mathcal{T}_e \omega_e b_e}{367.1 \rho_f g} \tag{16}$$

where ρ_f is the fuel density and b_e is the fuel consumption rate. The ICE power map, dependent on the ICE angular velocity, and the fuel consumption rate [g/kWh], dependent on the ICE angular velocity and torque, are shown in Fig. 6a and 6b, respectively.

2) ICE emission maps

The vehicle emission is affected by many factors such as engine type, driver, road characteristics among others [1]. For the sake of simplicity, the emission model in this paper is considering using static maps depending on the ICE velocity and torque. The CO and NO_x emission rate are $\dot{m}_{CO}$ [g/s] and $\dot{m}_{NO_x}$ [g/s], respectively, and can be found in Fig. 6c and Fig. 6d.

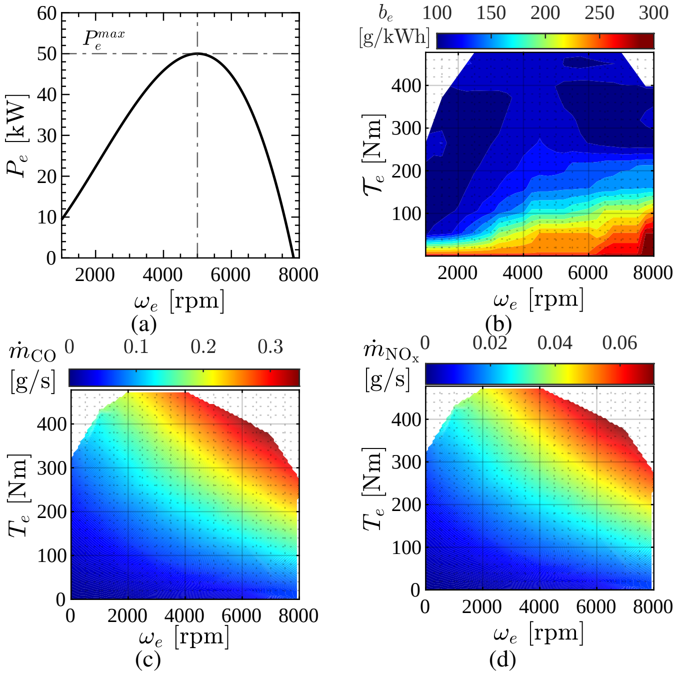

FIGURE 6. ICE maps: (a) power, (b) fuel consumption (b_e), (c) CO emission and (d) NO_x emission.

III. SIGMOID-CEEMD ENERGY MANAGEMENT

The proposed EMS is shown in Fig. 1. The low frequency demand, calculated by the CEEMD strategy, is shared between the ICE and the LIB according sigmoid functions optimized by the PSO algorithm. The UC controls the dc-link voltage while a phase-lag compensator (PLC) restores its terminal voltage.

A. POWER ALLOCATION BASED ON CEEMD AND PE

The EMD algorithm decomposes a signal into different time-scale characteristics without the need for predetermined harmonic orders or basis functions, as required in Fourier and WT, yielding a series of intrinsic mode functions (IMFs) [3]. The EMD method in [28] decomposes an original input signal by considering its local maxima and minima values through a shifting process. Initially, an upper envelope formed by the local maxima and a lower envelope formed by the local minima of the original signal are constructed. Therefore, the first component denoted $\psi_1[n]$ is defined as:

$$\psi_1[n] = u[n] - m_1[n] \tag{17}$$

with $u[n]$ the input signal and $m_1[n]$ the average signal between these envelopes. The shifting is repeated p times, considering the component obtained from the previous process as the original signal:

$$\psi_{11}[n] = \psi_1[n] - m_{11}[n] \tag{18}$$
$$\psi_{1p}[n] = \psi_{1(p-1)}[n] - m_{1p}[n] \tag{19}$$

This article has been accepted for publication in IEEE Open Journal of the Industrial Electronics Society. This is the author's version which has not been fully edited and content may change prior to final publication. Citation information: DOI 10.1109/OJIES.2025.3559447

where m_{1p} is the p-th envelope used. Therefore, defining $\mathrm{IMF}_1[n] = \psi_{1p}[n]$ as the first IMF component, the first residue $r_1[n]$ is calculated as:

$$r_1[n] = u[n] - \mathrm{IMF}_1[n]. \tag{20}$$

The process is then repeated considering $r_1[n]$ as the original signal until the standard deviation between two consecutive shifting results is less than a threshold. At the end of K repetitions, the same number of IMFs is obtained.
Definition 1: The operator denoted $\mathcal{E}_k(\cdot)$ extracts the k-th mode of the input signal, i.e., its k-th IMF using the EMD decomposition.

1) Complete ensemble empirical mode decomposition

To suppress the modal aliasing effect without affect the signal properties, the CEEMD inserts white noises to the original signal $u[n]$ [29]. Different realizations of white noise $w^h[n]$, of finite standard deviation $\sigma \in (0\ \ 1)$, are added to the signal to obtain:

$$u^h[n] = u[n] + w^h[n] \tag{21}$$

with $h = \{1, \cdots, H\}$ and the first IMF calculated as:

$$\mathrm{IMF}_1[n] = H^{-1} \sum_{h=1}^{H} \mathcal{E}_1\left(u^h[n]\right) \tag{22}$$

which allows to calculate the first residues and the second IMF by new decomposition as:

$$r_1[n] = u[n] - \mathrm{IMF}_1[n] \tag{23}$$

$$\mathrm{IMF}_2[n] = H^{-1} \sum_{h=1}^{H} \mathcal{E}_1\left(r_1[n] + \epsilon_1 \mathcal{E}_1\left(w^h[n]\right)\right) \tag{24}$$

where ϵ_1 is the ratio of data versus noise. For $k = \{1, \cdots, K\}$ the k-th residue is calculated as $r_k[n] = r_{(k-1)}[n] - \mathrm{IMF}_k[n]$ and the $(k+1)$-th mode is [29]:

$$\mathrm{IMF}_{(k+1)}[n] = H^{-1} \sum_{h=1}^{H} \mathcal{E}_1\left(r_k[n] + \epsilon_k \mathcal{E}_k\left(w^h[n]\right)\right) \tag{25}$$

and the process is finished when the final residue $r_K[n]$ is less than an established threshold, satisfying:

$$u[n] = r_K[n] + \sum_{k=1}^{K} \mathrm{IMF}_k[n]. \tag{26}$$

Let $\mathcal{P}[n] \in \mathbb{R}^{1\times N}$, with $n = \{1, \cdots, N\}$, be the sequence of the HEV power demand $P_d(t)$, for $t \in [0\ \ t_{\max}]$. Therefore, the CEEMD in this paper is applied considering $u[n] = \mathcal{P}[n]$.

2) Permutation entropy

The application of the CEEMD algorithm in the HEV power demand produces a set of K IMFs, as described in (26). Each sequence $\mathrm{IMF}_k[n]$ presents a level of complexity that is related with its frequency response. Therefore, the high and low frequency IMF sequences are separated according to the PE.

Considering the embedding dimension $2 \leq m \in \mathbb{N}$ and the time delay τ, the power demand of the k-th IMF sequence $\mathrm{IMF}_k[n] = \{\mathrm{imf}_k^n\}_{n=1}^N = \left\{\mathrm{imf}_k^1, \mathrm{imf}_k^2, \cdots, \mathrm{imf}_k^N\right\}$ can be written as the embedding vector [45]:

$$v = \left\{\mathrm{imf}_k^1, \mathrm{imf}_k^{1+\tau}, \cdots, \mathrm{imf}_k^{1+(m-1)\tau}\right\}. \tag{27}$$

Then, the m elements of the embedding vector are rearranged in ascending order [3], [45]:

$$\mathrm{imf}_k^{n+(q_1-1)\tau} \leq \mathrm{imf}_k^{n+(q_2-1)\tau} \leq \cdots \leq \mathrm{imf}_k^{n+(q_m-1)\tau} \tag{28}$$

where $q_1, q_2, \cdots, q_m$ is the column where each element is located, which allows mapping any embedding vector v into the space mapping vector $\{q_1, q_2, \cdots, q_m\} \in \mathbb{N}^m$ [45]. In a variety of arrangements, there are m spacing mapping vectors with probability of occurrence $p_1, p_2, \cdots, p_s$, with $s \leq m!$. Therefore, the normalized PE is calculated as [3]:

$$\chi(m,\tau) = -\frac{\sum_{i=1}^{s} p_i(\tau)\ln(p_i(\tau))}{\ln(m!)}. \tag{29}$$

To analyze the k-th IMF frequency characteristics according to its PE denoted χ_k, with $k = \{1, \cdots, K\}$ and calculated according (29), the larger the value of χ_k the less regular is the sequence, i.e., IMFs with higher PE values are signals more complex, and then regarded as high frequency demand [3]. Therefore, the low frequency power demand and the reference power for the LIB and ICE are calculated as:

$$P_{\mathrm{LF}} = \sum_k \mathrm{IMF}_k[n] \quad / \quad \chi_k(\mathrm{IMF}_k, \tau) \leq \sigma \tag{30}$$

$$P_{b\mathrm{ICE}}^{*} = P_{\mathrm{LF}} + \Delta v_{uc} \tag{31}$$

where Δv_{uc} is a term for UC terminal voltage restoration, which will be discussed later.

B. ICE MANAGEMENT

To avoid discontinuities in the EMS, which can lead to undesirable high frequency oscillations, the sigmoid functions are employed to calculate the ICE reference power as:

$$P_{\mathrm{ICE}}^{*} = \alpha\left(P_o + \mathrm{DoD}_b \underbrace{(\mathcal{S}_{\mathrm{low}} + \mathcal{S}_{\mathrm{high}})}_{\Delta P_{\mathrm{ICE}}}\right) \tag{32}$$

where $\mathrm{DoD}_b \triangleq 1 - \mathrm{SoC}_b$, $\alpha \in [0\ \ 1]$ is a gain to be defined and $\mathcal{S}_{\mathrm{low}}$ and $\mathcal{S}_{\mathrm{high}}$ are sigmoid functions to produce displacements around the low rotation reference power P_o, calculated as:

$$P_o = \frac{P_o^{\mathrm{A}}}{1 + e^{-\kappa(\mathrm{SoC}_b - \mathrm{SoC}_{\max})}} + \frac{P_o^{\mathrm{B}}}{1 + e^{\kappa(\mathrm{SoC}_b - \mathrm{SoC}_{\max})}} \tag{33}$$

where κ is the sigmoid steepness and $P_o^{\mathrm{A}}, P_o^{\mathrm{B}} \in \mathbb{R}_+$ are design parameters so that $P_o^{\mathrm{A}} < P_o^{\mathrm{B}}$. When $\mathrm{SoC}_b \geq \mathrm{SoC}_{\max}$ the lower rotation demand is defined as the minimum value P_o^{A}. However, if $\mathrm{SoC}_b \leq \mathrm{SoC}_{\max}$, the lower rotation demand is defined as P_o^{B} (see Fig. 7a).

This article has been accepted for publication in IEEE Open Journal of the Industrial Electronics Society. This is the author's version which has not been fully edited and content may change prior to final publication. Citation information: DOI 10.1109/OJIES.2025.3559447

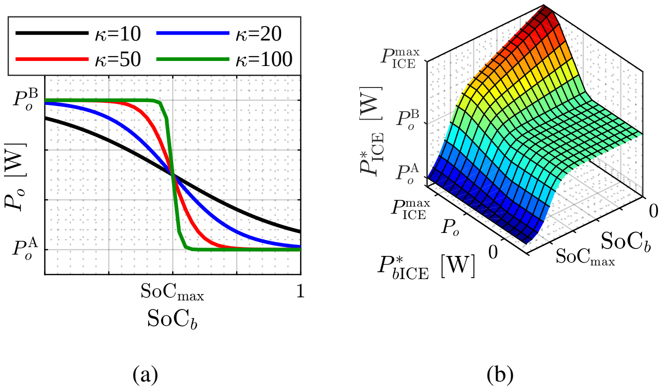

FIGURE 7. ICE management: (a) low rotation reference power and (b) total reference power.

The sigmoid functions $\mathcal{S}_{\text{low}}$ and $\mathcal{S}_{\text{high}}$ in (32), used to calculate the displacement Δi_{ICE}, are given by:

$$\mathcal{S}_{\text{low}} = \frac{P^*_{b\text{ICE}} - P_o}{1+e^{-\kappa_m\left(P^*_{b\text{ICE}} - P_o\right)}} \frac{1}{1+e^{-\kappa_m\left(P^{\max}_{\text{ICE}} - P^*_{b\text{ICE}}\right)}} \tag{34a}$$

$$\mathcal{S}_{\text{high}} = \frac{\left(P^{\max}_{\text{ICE}} - P_o\right)}{1+e^{\kappa_m\left(P^{\max}_{\text{ICE}} - P^*_{b\text{ICE}}\right)}} \tag{34b}$$

where $P^{\max}_{\text{ICE}}$ is the ICE maximum power. When $P^*_{b\text{ICE}} \leq P_o$, the ICE reference power is $P^*_{\text{ICE}} = P^{\text{B}}_o$ when $\text{SoC}_b \leq \text{SoC}_{\max}$ (green plateau in Fig. 7b). Moreover, when $P_o \leq P^*_{b\text{ICE}} \leq P^{\max}_{\text{ICE}}$, the ICE reference power is approximately linear with respect to the demand $P^*_{b\text{ICE}}$. Otherwise, if the demand is higher than $P^{\max}_{\text{ICE}}$, the reference is limited to this value.

Once the ICE power reference is set, a triple control loop strategy is employed to determine the angular opening of the butterfly valve. The inner angular control loop (Fig. 8a) must be faster than the speed control loop (Fig. 8b) which, in turn, should be faster than the outer power control loop (Fig. 8c) to ensure effective control performance. This hierarchical control was achieved through the appropriate selection of the PI_p, PI_ω and PI_θ controllers gains, ensuring that the open-loop cutoff frequency of the speed control loop (L_ω) is approximately 0.5 to 1 decade lower than that of the angular control loop (L_θ), while the open-loop cutoff frequency of the power control loop (L_P) is approximately 0.5 to 1 decade lower than that of the speed control loop.

C. LIB MANAGEMENT

Once the ICE reference power is defined, the LIB reference power P^*_b is calculated as:

$$P^*_b = P^*_{b\text{ICE}} - P^*_{\text{ICE}}. \tag{35}$$

Remark 3: Substituting (32) in (35) it is possible to see that the gain α defines whether the ICE or LIB is more used to supply the lower frequency demand in (30). Higher values of α result in greater use of the ICE, while lower α result in greater use of the LIB.

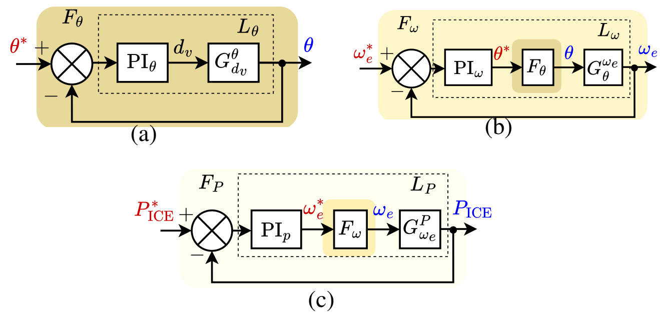

FIGURE 8. ICE butterfly triple control loop: (a) angle control loop, (b) angular velocity control loop and (c) power control loop.

D. ULTRACAPACITOR MANAGEMENT

The high frequency demand is designated as reference for the UC, due to its high power density, by using the dc-link voltage v_{dc}, its reference v^*_{dc} and a voltage control loop as:

$$i^*_{uc} = \text{PI}_{v_{dc}}\left(v^*_{dc} - v_{dc}\right) \tag{36}$$

where $\text{PI}_{v_{dc}}$ is a PI controller with proportional and integral gains k^{dc}_p and k^{dc}_i, respectively.

1) Voltage restoration

To restore the UC terminal voltage after power peaks, a PLC $\text{PL}_{v_{uc}}$ is used. The PLC is chose to improve the stationary response without affect the transient response, i.e., to increase the gain at low frequencies without significantly affect the root locus in the vicinity of the closed-loop poles. Therefore, the voltage error is used to calculate the signal:

$$\Delta v_{uc} = \underbrace{\left(\frac{\beta_u \tau_u s + \beta_u}{\beta_u \tau_u s + 1}\right)}_{\text{PL}_{v_{uc}}} \left(v^*_{uc} - v_{uc}\right) \tag{37}$$

where τ_u is the zero time constant and β_u is the low-frequency gain. The control signal Δv_{uc} is used in (31).

When compared to the traditional PI strategy, the PLC presents reduced low-frequency gain, which relaxes the voltage restoration. However, the phase delay does not affect significantly the transient response if the pole and zero are sufficiently close. In relation to the LPF, the PLC tuning method is improved due to the higher degree of freedom. Moreover, the LPF presents a trade-off between low-frequency gain and cut-off frequency.

The control signal for UC voltage restoration is incorporated as a reference for both the LIB and the ICE in (31). However, since the UC is a fast dynamic source, employing a PI controller may result in high-frequency demands on the LIB and ICE, which is undesirable. Therefore, to ensure that the PLC does not significantly affect the transient response of the controlled system, the pole $(-1/\beta_u\tau_u)$ and zero $(-1/\tau_u)$ in (37) must be positioned close to each other. Furthermore, the improvement in steady-state error is directly proportional to the ratio between the zero and the pole, i.e., the value of β_u. Therefore, to achieve a substantial reduction in steady-state error while maintaining the transient response, the pole and zero of the PLC should be located near the origin.

E. PARTICLE SWARM OPTIMIZATION

To optimize the HEV operation, the PSO, a population-based on the stochastic algorithm characterized by high versatility and flexibility [46], is applied. The PSO algorithm seeks to find the value $x^* = \left[\alpha \;\; P_o^{\mathrm{A}} \;\; P_o^{\mathrm{B}}\right]$ that minimizes an objective function $\mathcal{F}(x) : \mathbb{R}^d \to \mathbb{R}$ by introducing N_p particles into the search space with positions $x_k \in \mathbb{R}^d$, moving towards its personal best and global position with velocities $v_k \in \mathbb{R}^d$, $k = \{1, 2, \cdots, N_p\}$. Starting from the initial conditions x_k^0 and v_k^0, the position and velocity of each particle are updated according to

$$\begin{cases} x_k^{n+1} = x_k^n + v_k^{n+1} \\ v_k^{n+1} = v_k^n + c_1 R_1^n \left(y_k^n - x_k^n\right) + c_2 R_2^n \left(\overline{y}_k^n - x_k^n\right) \end{cases} \tag{38}$$

where $c_1, c_2 \in \mathbb{R}$ are acceleration coefficients, R_1^n, $R_2^n \in [0 \;\; 1]$ are random numbers, y_k^n and $\overline{y}_k^n$ are the best position of particle k and of all particles at iteration n, respectively, calculated as:

$$y_k^{n+1} = y_k^n + 0.5\left(x_k^{n+1} - y_k^n\right) \mathbb{S}\left(x_k^{n+1},\; y_k^n\right) \tag{39}$$

$$\overline{y}_k^{n+1} = \operatorname{argmin}\left\{\mathcal{F}(y_1^{n+1}), \mathcal{F}(y_2^{n+1}), \cdots, \mathcal{F}(y_{N_p}^{n+1})\right\} \tag{40}$$

where the operator $\mathbb{S}(a, b) \triangleq 1 + \operatorname{sign}\left[\mathcal{F}(b) - \mathcal{F}(a)\right]$ [46]. The PSO finds the optimum solution that minimizes the compromise among fuel consumption, LIB aging and SoC limits according to

$$\min_x \quad \mathcal{F}(x) = \int_0^{t_{\max}} \Upsilon_m \dot{m}_f + \Upsilon_s \dot{\mathrm{S}}\mathrm{oH}_b \tag{41a}$$

$$\text{s.t.} \quad \mathrm{SoC}_{\min} \leq \mathrm{SoC}_b \leq \mathrm{SoC}_{\max} \tag{41b}$$

$$0 \leq \alpha \leq 1 \tag{41c}$$

$$0 \leq P_o^{\mathrm{A}} \leq P_o^{\mathrm{B}} \leq P_e^{\max} \tag{41d}$$

$$\overline{m}_{\mathrm{CO}} < \; k_{\mathrm{CO}} \overline{m}_{\mathrm{CO}}^{\mathrm{ICE}} \tag{41e}$$

$$\overline{m}_{\mathrm{NO_x}} < \; k_{\mathrm{NO_x}} \overline{m}_{\mathrm{NO_x}}^{\mathrm{ICE}} \tag{41f}$$

where Υ_m and Υ_s are compromised weights between fuel consumption and LIB aging to solve the multiobjective optimization, $\overline{m}_{\mathrm{CO}}$ and $\overline{m}_{\mathrm{NO_x}}$ are the CO and $\mathrm{NO_x}$ emission rate [g/km], respectively, and $\overline{m}_{\mathrm{CO}}^{\mathrm{ICE}} = 3.67$ g/km and $\overline{m}_{\mathrm{NO_x}}^{\mathrm{ICE}} = 0.81$ g/km are the medium and heavy-duty ICE average emissions [6], while the gains $k_{\mathrm{CO}}, k_{\mathrm{NO_x}} \in [0 \;\; 1]$ define the desired emission reduction, i.e., the higher the gains are the more relaxed the constraints become.

The influence of the PSO on the sigmoid functions is illustrated in Fig. 9. For a fixed value of P_o^{B}, as the PSO increases P_o^{A}, the difference between the maximum and minimum power of the ICE decreases, indicating that its operation occurs with reduced power variation (see Fig. 9a). Conversely, when P_o^{A} is fixed and P_o^{B} increases, the opposite behavior is observed (see Fig. 9b). Higher values of

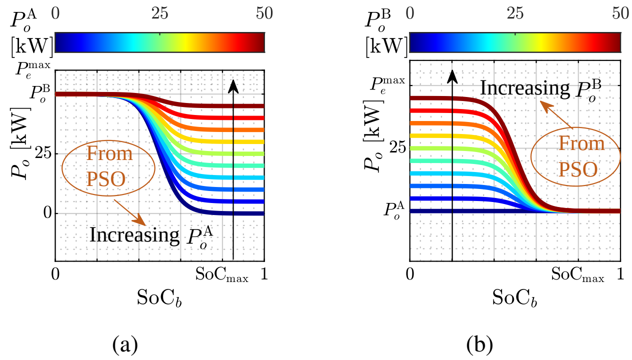

FIGURE 9. PSO influence in the ICE sigmoid functions: increasing (a) P_o^{A} and (b) P_o^{B}.

P_o^{A} and P_o^{B} demand greater power from the ICE, thereby relieving the load on the LIB. Furthermore, since the gain α multiplies both sigmoid functions in (32), higher α values increase the difference between the ICE's operational points.

IV. NUMERICAL AND EXPERIMENTAL RESULTS

In this section, the performance of the proposed sigmoid-based particle swarm optimization strategy is verified using numerical simulations and a real-time hardware-in-the-loop (HIL) platform composed of the Speedgoat™, where the S-HEV plant is built, and the dSPACE™, where the strategy is implemented, as shown in Fig. 10a.

The dSPACE1006 multiprocessor system, equipped with an AMD Opteron™ processor, acquires analog measurements from the Speedgoat via the 16-bit A/D board DS2004 and produces the PWM signals through the digital board DS4004. On the other hand, the S-HEV measurements are collected from Speedgoat (performance core Intel®Core™ i3 FPGA 100k) using the 16-bit analog output board IO110, while the PWM signals are received through the digital board IO316. The schematic of the board connections is shown in Fig. 10b.

The results were obtained considering three drive cycles with different characteristics regarding velocity, travel distance (L_d), average velocity ($\overline{v}_x$) and duration. The selected drive cycles were the SC03, HWYCOL and the Brazilian real-world drive cycle between the cities of Campinas and São Paulo (see Fig. 11a), collected and presented by Miranda et al. [39]. The speed profile of the drive cycles are shown in Fig. 11b and the emission constraints (41e) and (41f) are disregarded unless stated otherwise.

The LIB stress analysis is done by the power decomposition in low (A_w) and high frequency (D_w) components using the Haar Wavelet decomposition, described in [23]. The high frequency component standard deviation σ_w, around the null average value, indicates the utilization of the LIB [47]. The electrical and control parameter are described in Table 2 and Table 3. The total operational cost [\$/100 km] is calculated as:

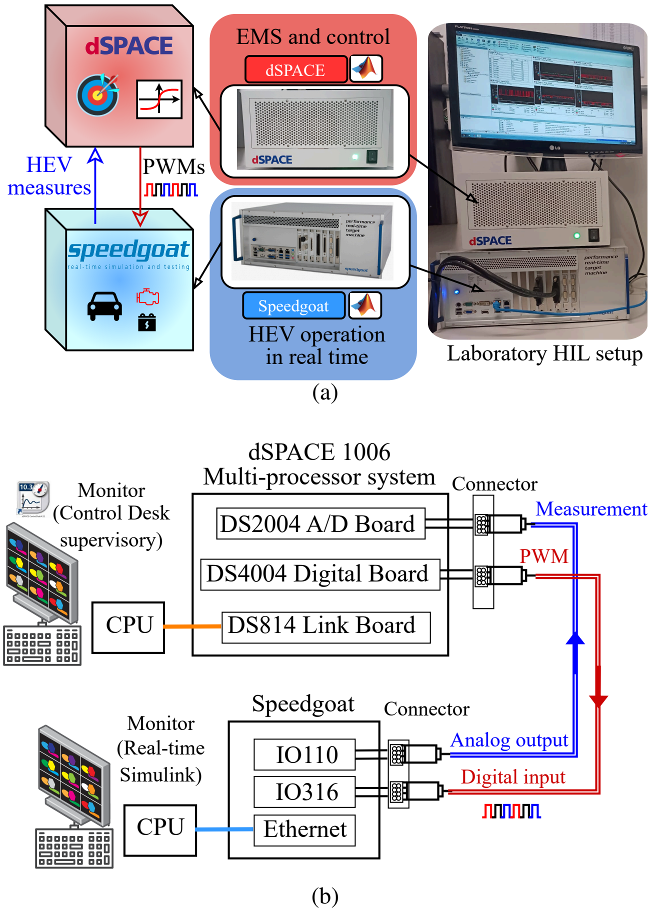

FIGURE 10. Real-time HIL setup: (a) Lab prototype and (b) Schematic of board connections.

$$\text{Cost} = \frac{100}{\mathrm{L}_d}\left(\mathrm{E}_b\beta_b + \mathrm{F}_c\beta_f + \left(1 - \mathrm{SoH}_b^{\mathrm{end}}\right) C_b\beta_{\mathrm{LIB}}\right) \tag{42}$$

where E_b [kWh] is the LIB energy with associated cost $\beta_b = 0.13$ \$/kWh [48][1], F_c [ℓ] is the ICE fuel consumption with associated cost $\beta_f = 1.08$ \$/ℓ[2], $\mathrm{SoH}_b^{\mathrm{end}}$ is the final LIB SoH, C_b [kWh] is the LIB capacity, $\beta_{\mathrm{LIB}} = 124.24$ \$/kWh [38] is the LIB pack price and $\mathrm{L}_d = \int_0^{t_{\max}} v_x$ is the distance.

A. RESULTS FOR THE BRAZILIAN REAL WORLD DRIVE CYCLE

By applying the CEEMD algorithm to decompose the power demand in the Brazilian real-world drive cycle, $K = 28$ IMFs were obtained. Some of the produced IMFs are shown in Fig. 12a, while the CEEMD algorithm diagram is shown in Fig. 12b. Higher orders IMFs are sequences of lower frequency, which can be confirmed by analyzing the PE in Fig. 13. The IMF_k for $k \geq 22$ present PE less than the white noise standard deviation σ and, therefore, are used to calculate the low frequency demand.

[1] 1€ for 1.11\$

[2] Brazilian average price in September 2nd, 2024

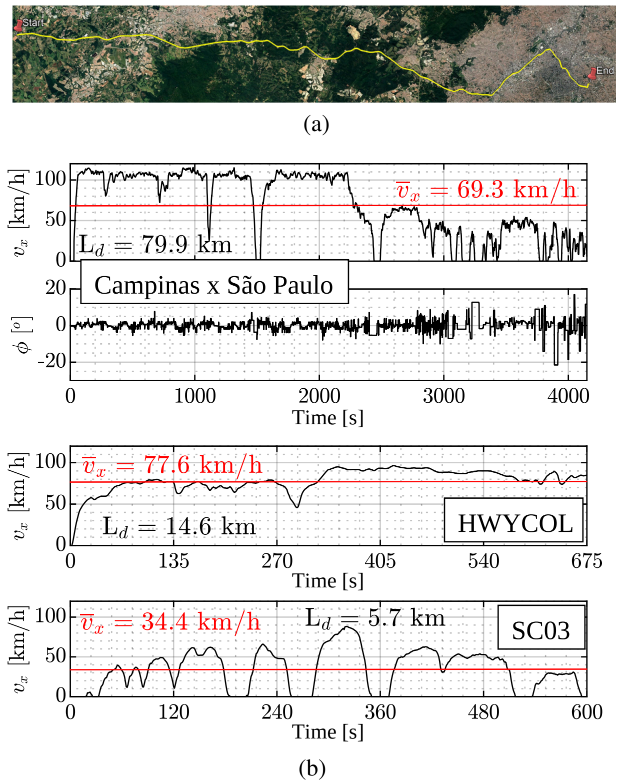

FIGURE 11. Drive cycles: (a) Brazilian drive-cycle path [39] and (b) speed profile for all drive cycles.

The first scenario compares the nominal operation with ICE+LIB, while the second scenario considers the LIB is the main source, with P^*_{ICE} set as the minimum value P_o in (33). As can be seen in Fig. 14, the UC power presents faster dynamic compared to the LIB power. When the LIB is the main source, it delivers a higher power, which leads to an excessive discharge of the device, reaching $\mathrm{SoC}_b \leq \mathrm{SoC}_{\min}$. Consequently, the LIB temperature increase and the SoH is strongly reduced in relation to the nominal operation (LIB lifetime 23 times smaller). Moreover, the UC and dc-link voltages are restored to their reference values. Additionally, the LIB voltage and current, the UC current and the butterfly valve angle are shown in Fig. 15. The LIB c-rate is 1.28 times bigger when the ICE is underutilized, which increases the LIB usage and stress.

B. UC VOLTAGE RESTORATION

To verify the effectiveness of the proposed strategy under other drive cycles and evaluate the UC terminal voltage restoration, the PLC was compared with traditional LPF and PI methods found in the literature under the HWYCOL drive cycle in numerical results performed in Matlab® and Simulink® environment. Although the UC voltage integral absolute error (IAE) is lower for the LPF and PI strategies (see Fig. 16b), the LIB power presents higher dynamic (see Fig. 16a). In addition, the LIB stress is reduced with the PLC by relaxing the voltage restoration, demonstrated by

TABLE 2. HEV main parameters.

Parameter	Symbol	Value
Vehicle		
Total mass	M_v	$4,000$ kg
Aerodynamic drag	C_d	2
Front area	A_v	7.0 m^2
Density	ρ_a; ρ_f	1.29; 815 kg/m^3
Shaft stiffness	K_{sh}; K_{sl}	$131,780$; $487,587$ Nm
Shaft damping	B_{sh}; B_{sl}	$4,666$; $17,266$ Nms
Reducer efficiency	η_r	95%
Reducer inertia	J_r	0.005 kgm^2
Load inertia	J_m	80.125 kgm^2
Load friction	B_m	0.005 Nms
Wheels radius	r_d	0.28 m
Tire ratio rate	r_L/r_d	0.98
Slip stiffness	c_κ	16
Friction coefficient	f_F	0.020
Reducer ratio	i_r	3.7
Lithium-ion battery and Ultracapacitor		
LIB capacity	C_b	120 Ah
Polarization capacitor	C_1	$15,721.5$ F
Heat conduction	R_c; R_u	182.36; $1,410$ KW^{-1}
Thermal capacitances	C_c; C_s	10 kJK^{-1}; 50 kJK^{-1}
UC capacitance	C_{uc}	2 F
UC resistance	R_{ou}	50 mΩ
Internal combustion engine and generator		
Maximum power	$P_e^{\max}$	50 kW
Velocity for $P_e^{\max}$	ω_{pp}	$5,000$ rpm
	γ_1	0.6526
Model coefficients	γ_2	1.6948
	γ_3	-1.3474
Valve dc source	v_s	12.0 V
dc motor gain	K_m	19.3 rpm/V
Chopper PWM gain	K_c	0.12 V/%
Motor time constant	τ_m	0.052 s
Valve delay	τ_v	0.01 s
Rectifier efficiency	η_r	97%
Inertias	J_e; J_g	0.005 kgm^2
BBC converters and dc-link		
Inductances	L_b; L_u	10 mH; 5 mH
Inductor resistances	r_b; r_u	100 mΩ; 50 mΩ
Switches resistance	r_s	30 mΩ
Switching frequency	f_s	20 kHz
dc-link capacitance	C_{dc}	$3,000$ μF

TABLE 3. EMS and control parameters.

Parameter	Symbol	Value
ICE PI$_p$ controller	$\mathcal{K}_p^{\mathrm{p}}$; $\mathcal{K}_i^{\mathrm{p}}$	1 $\frac{\mathrm{rpm}}{\mathrm{W}}$; 3 $\frac{\mathrm{rpm}}{\mathrm{Ws}}$
ICE PI$_\omega$ controller	$\mathcal{K}_p^{\omega}$; $\mathcal{K}_i^{\omega}$	0.5 $\frac{\mathrm{rad}}{\mathrm{rpm}}$; 2 $\frac{\mathrm{rad}}{\mathrm{srpm}}$
ICE PI$_\theta$ controller	$\mathcal{K}_p^{\theta}$; $\mathcal{K}_i^{\theta}$	0.1 $\frac{1}{\mathrm{rad}}$; 0.3 $\frac{1}{\mathrm{srad}}$
LIB PI$_{i_b}$ controller	$\mathcal{K}_p^{i_b}$; $\mathcal{K}_i^{i_b}$	0.1 $\frac{1}{\mathrm{A}}$; 1.0 $\frac{1}{\mathrm{sA}}$
dc-link PI$_{v_{dc}}$ controller	$\mathcal{K}_p^{v_{dc}}$; $\mathcal{K}_i^{v_{dc}}$	1.0 $\frac{1}{\Omega}$; 3.0 $\frac{1}{\Omega\mathrm{s}}$
UC PL$_{v_{uc}}$ controller	β_u; τ_u	10; 10 rad/s
UC PI$_{i_{uc}}$ controller	$\mathcal{K}_p^{i_{uc}}$; $\mathcal{K}_i^{i_{uc}}$	0.1 $\frac{1}{\mathrm{A}}$; 1.0 $\frac{1}{\mathrm{sA}}$
LIB SoC limits	SoC$_{\min}$; SoC$_{\max}$	0.4; 0.8
Sigmoid steepness	κ; κ_m	20; 0.05
PSO coefficients	c_1; c_2; N_p; Υ_m; Υ_s	2.05; 2.05; 40; 2; 5

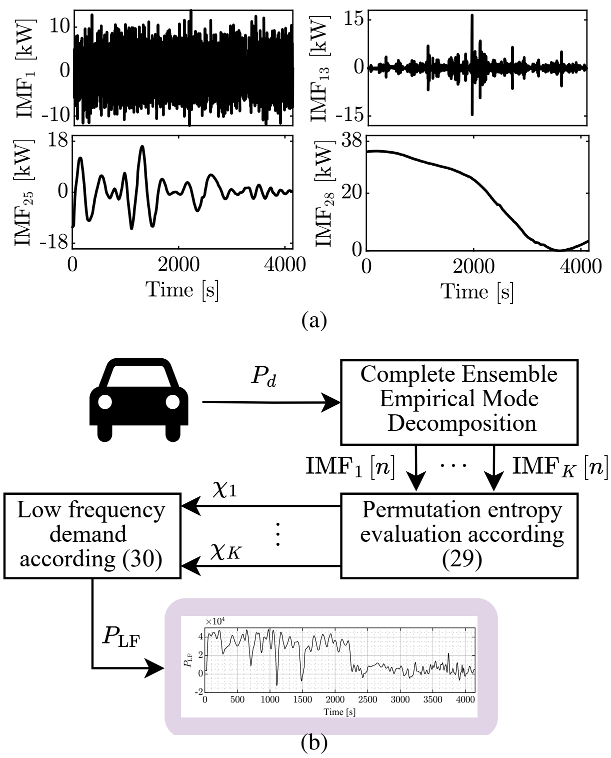

FIGURE 12. CEEMD algorithm: (a) IMF_1, IMF_{13}, IMF_{25} and IMF_{28} and (b) low frequency demand evaluation.

the lowest standard deviation σ_w of the LIB power detail coefficient D_w by using the WT (see Fig. 16e, Fig. 16f and Fig. 16g).

The LIB voltage, current, and duty cycle are presented in Fig. 17, alongside the corresponding UC current and duty cycle. It is evident that the dynamic behavior of the UC current is more pronounced than that of the LIB, as expected. Furthermore, the LIB current peak observed for the LPF and PI strategies is nearly twice that of the PLC strategy (zoomed-in region in Fig. 17b), which explains the reduced stress associated with the PLC strategy.

Remark 4: The PI controller for the UC voltage restoration comparison was tuned for a 20 dB/decade attenuation up to 0.4 Hz to balance low-frequency gain and cut-off frequency, with $k_p = 2.0$ and $k_i = 5.0$. Similarly, the LPF time constant was set to a frequency 0.05 Hz.

C. COMPARISON WITH THE LITERATURE

In this section, the proposed SPSO-CEEMD strategy is compared with other methods in the literature. The IT2-FLC in [15], originally designed for a P-HEV, was adapted to application in the S-HEV. As shown in Fig. 18a, the dc-link control and UC management are the same as the proposed in Section III-D. A traditional FLC estimates the optimum ICE torque ($\tau_{\mathrm{ICE}}^{\mathrm{op}}$) according to the power demand P_d and the IT2-FLC defines the gain $\alpha \in [0\ \ 1]$ that split the torque demand between the LIB and the ICE. Moreover, the XOS in [16] was also adapted, as shown in Fig. 18b. For the SC03 drive cycle, the IT2-FLC strategy charge more the LIB with the ICE during the drive cycle, which leads to the more

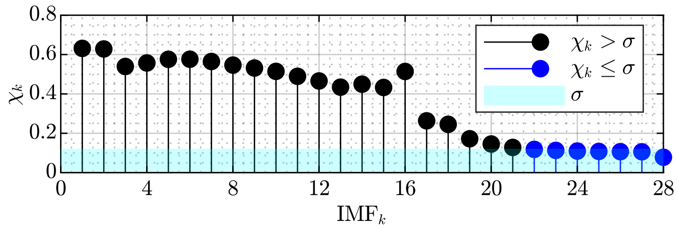

FIGURE 13. PE of each IMF obtained by the CEEMD algorithm.

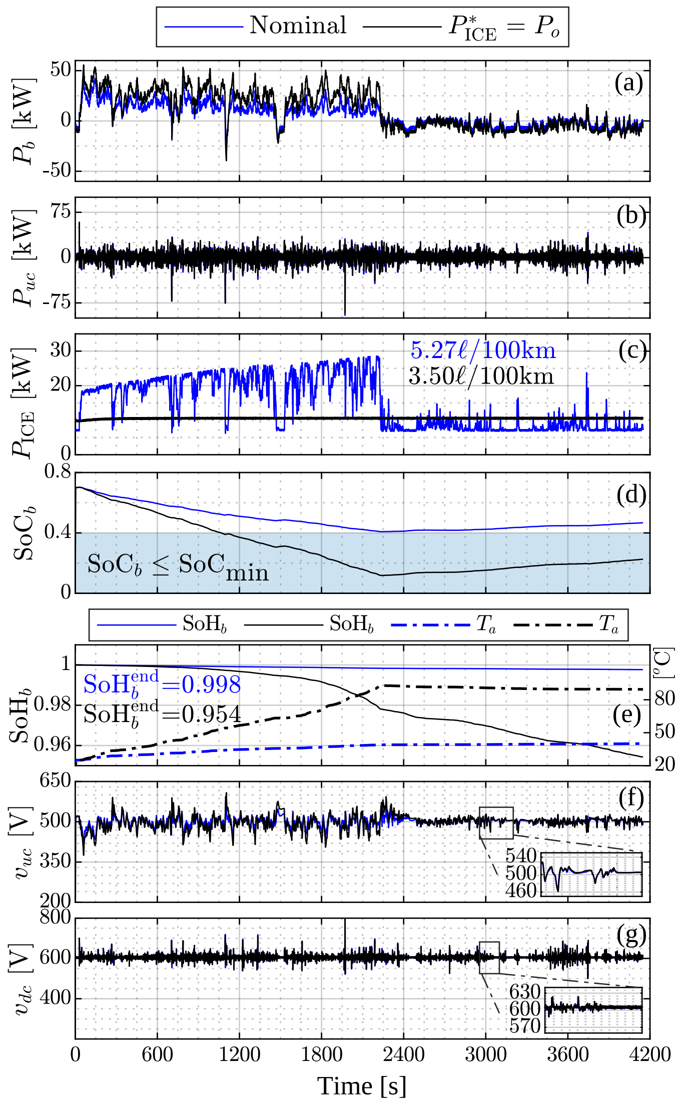

FIGURE 14. Brazilian real-world drive cycle experimental results: (a) LIB power, (b) UC power, (c) ICE power, (d) LIB SoC, (e) LIB SoH and temperature, (f) UC voltage and (g) dc-link voltage.

fuel consumption (see Fig 19a and Fig 19c). However, the ICE restarts are reduced in relation to the XOS strategy (see Fig 19d). The proposed SPSO-CEEMD strategy keeps the ICE on during all the with intermediary fuel consumption.

Figure 20a confirms that the LIB is discharged often with the IT2-FLC strategy, which leads to a positive LIB energy

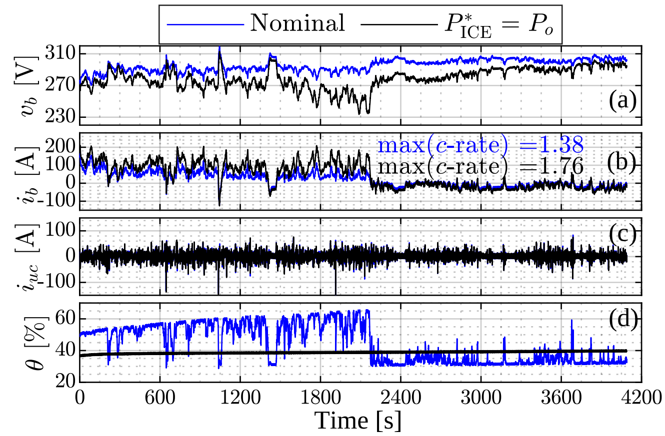

FIGURE 15. Brazilian real-world drive cycle experimental results: (a) LIB voltage, (b) LIB current, (c) UC current and (d) butterfly valve angle.

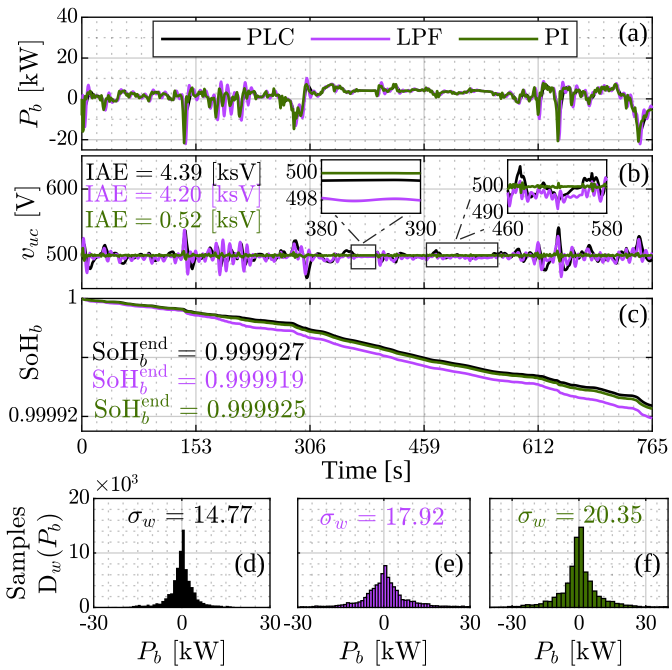

FIGURE 16. UC voltage restoration comparison under the HWYCOL drive cycle: (a) LIB power, (b) UC voltage, (c) LIB SoH and Wavelet standard deviation of the detail coefficient using (d) PLC, (e) LPF and (f) PI

consumption (see Fig. 20k). The value SoH$_b^{\text{end}}$ is bigger and the final temperature T_a^{end} is lower with the proposed SPSO-CEEMD (see Fig. 20b, Fig. 20c), indicating a larger lifetime. Analyzing the LIB power detail coefficients D$_w$ obtained by the WT (see Fig. 20d, Fig. 20e, Fig. 20f) and the standard deviation σ_w (see Fig. 20g, Fig. 20h, Fig. 20i), it can be seen that the LIB stress is smaller with the proposed strategy. Moreover, the total cost in (42) for the proposed strategy is the lowest (see Fig 20l).

This article has been accepted for publication in IEEE Open Journal of the Industrial Electronics Society. This is the author's version which has not been fully edited and content may change prior to final publication. Citation information: DOI 10.1109/OJIES.2025.3559447

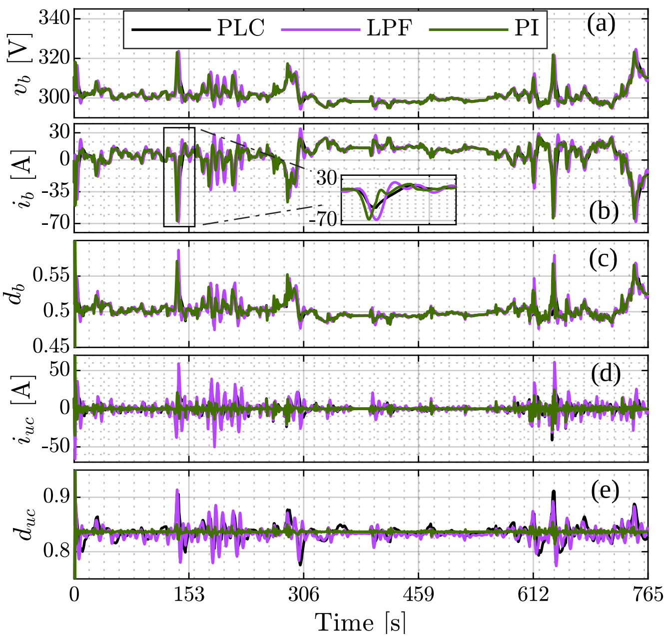

FIGURE 17. UC voltage restoration comparison under the HWYCOL drive cycle: (a) LIB voltage, (b) LIB current, (c) LIB duty-cycle, (d) UC current and (e) UC duty-cycle.

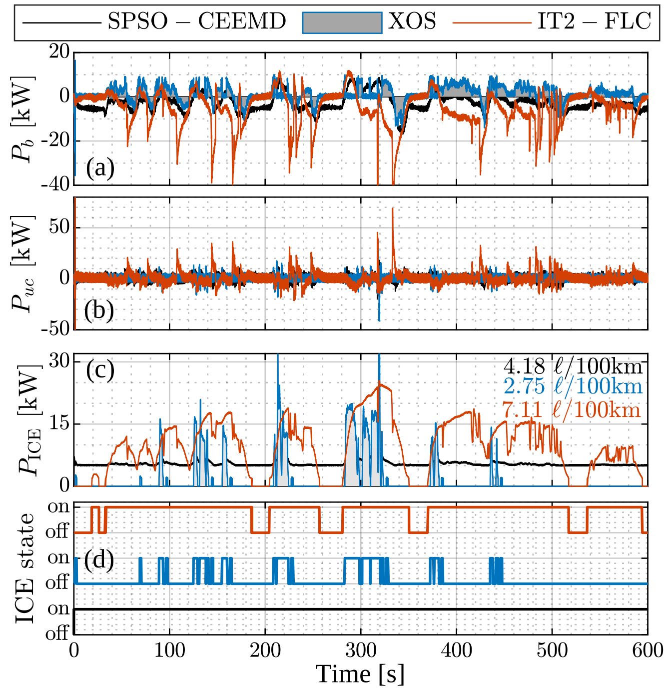

FIGURE 19. Experimental comparison for the SC03 drive cycle: (a) LIB power, (b) UC power, (c) ICE power and (d) ICE state.

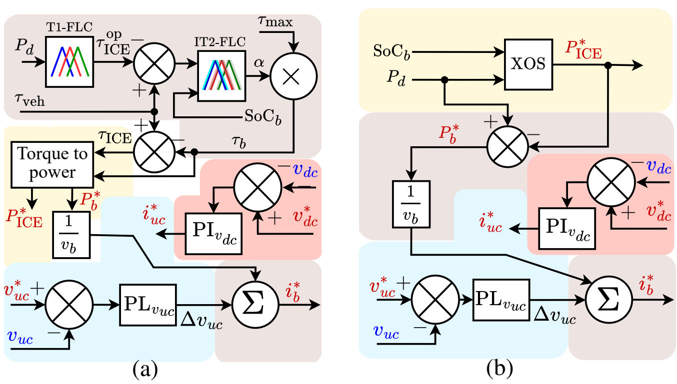

FIGURE 18. Block diagrams: (a) IT2-FLC adapted from [15] and (b) XOS adapted from [16].

D. TRADE-OFF BETWEEN FUEL SAVING AND EMISSIONS

In this section, the CO and NO_x emissions are taken into account by adding the constrains in the optimization problem in (41) for three different values of k_{CO} and k_{NO_x}. The ICE and LIB powers are shown in Fig. 21, where it is possible to see that for greater values of k_{CO} and k_{NO_x} the emission constraint are more relaxed, making the ICE be more used than the LIB. However, when the emission constraint is hard $k_{CO} = k_{NO_x} = 0.5$, the LIB power is greater.

To assess the effectiveness of emission optimization, Fig. 22 presents the average emissions of the constrained SPSO-CEEMD for different values of k_{CO} and k_{NO_x}, alongside the unconstrained SPSO-CEEMD and the IT2 and XOS methods adapted from the literature. As can be seen, the constraints on CO and NO_x emissions are satisfied for all values of k_{CO} and k_{NO_x}. Moreover, the numerical results for all scenarios are presented in Table 4, which demonstrates that emission reduction leads to increased LIB usage. For instance, setting $k_{CO} = k_{NO_x} = 0.5$ results in a 44.21% reduction in CO emissions and a 44.78% reduction in NO_x emissions. However, the final SoH analysis indicates that the LIB lifetime is 1.44 times longer when emission constraints are not considered.

V. CONCLUSION AND FUTURE WORKS

In this work, a CEEMD strategy is applied for the first time in a HEV to improve the LIB lifetime by avoiding high frequency demand during driving. The ICE is managed by sigmoid functions optimized by the PSO algorithm considering the trade-off between fuel consumption and LIB SoH, while incorporating the emission reduction as constraints of the optimization.

The ICE control is achieved through a triple control loop strategy, which regulates power, angular velocity, and the angle of the butterfly valve. The UC is responsible for the dc-link voltage control, with its terminal voltage restored by a PLC to keep the device available in the next power peaks demand.

The theoretical assessments, numerical and experimental results show that:

1) The CEEMD algorithm decomposes the power demand without definition of a basis function. With the proposed strategy, it is possible to use the CEEMD in

This article has been accepted for publication in IEEE Open Journal of the Industrial Electronics Society. This is the author's version which has not been fully edited and content may change prior to final publication. Citation information: DOI 10.1109/OJIES.2025.3559447

TABLE 4. Energy management comparison: numerical results.

		Fuel [ℓ/100km]	$\mathrm{SoH}_b^{\mathrm{end}}$	CO [g/km]	$\mathrm{NO_x}$ [g/km]	max (T_a) [°C]	max (c−rate)	F_c [$m\ell$]	Converters' efficiency [%]
Constrained SPSO-CEEMD	$k_{\mathrm{CO}} = k_{\mathrm{NO_x}} = 0.5$	1.30	0.9999354	1.83	0.37	25.20	0.69	73.96	97.12
	$k_{\mathrm{CO}} = k_{\mathrm{NO_x}} = 0.7$	3.26	0.9999495	2.52	0.57	25.17	0.61	186.10	97.31
	$k_{\mathrm{CO}} = k_{\mathrm{NO_x}} = 0.8$	4.08	0.9999500	2.90	0.63	25.13	0.54	232.30	97.37
Unconstrained SPSO-CEEMD		4.18	0.9999551	3.28	0.67	25.07	0.45	238	97.42
IT2-FLC		7.11	0.9998898	4.22	0.86	26.46	1.42	405	97.06
XOS		2.75	0.9999251	2.43	0.49	25.55	0.93	157	97.09

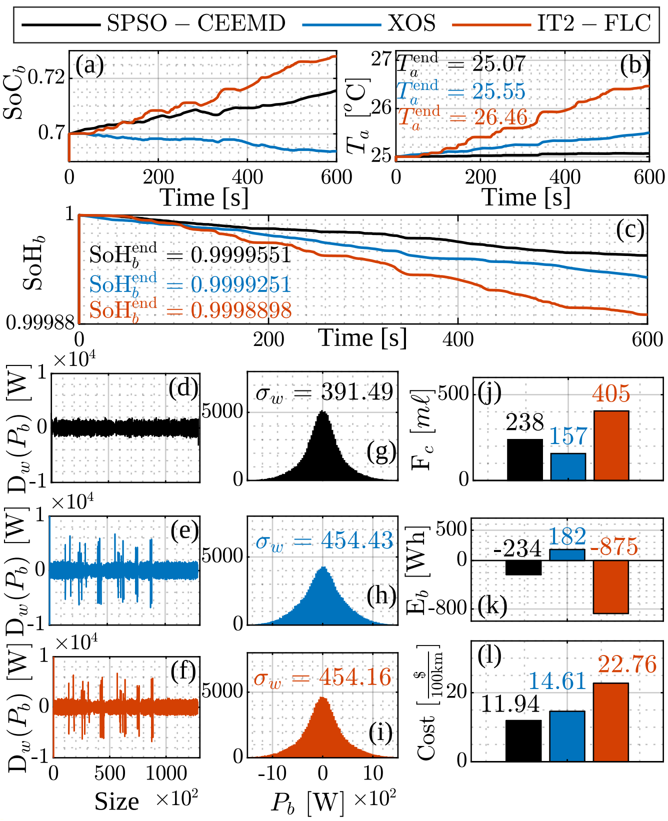

FIGURE 20. Experimental comparison for the SC03 drive cycle: (a) LIB SoC, (b) LIB temperature, (c) LIB SoH, Wavelet detail coefficient using (d) SPSO-CEEMD, (e) XOS, (f) IT2-FLC, detail coefficient standard deviation using (g) SPSO-CEEMD, (h) XOS, (i) IT2-FLC, (j) fuel consumption, (k) LIB energy and (l) cost.

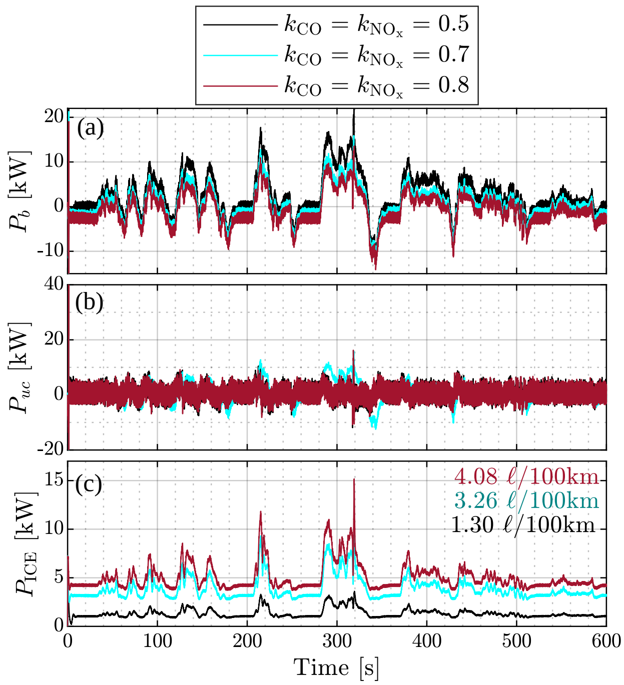

FIGURE 21. Experimental results for the SC03 drive cycle considering the emission constraints for different values of $k_{\mathrm{CO}} = k_{\mathrm{NO_x}}$: (a) LIB power, (b) UC power and (c) ICE power.

a HEV to define the low frequency component as reference for the LIB and ICE, which reduces the LIB aging and allow the ICE control;

2) The sigmoid functions allow the ICE control considering the butterfly valve slow dynamic and avoid discontinuities. Furthermore, the sigmoid optimization by the PSO algorithm reduces the fuel consumption and LIB aging for a real world Brazilian drive cycle, the SC03 and the HWYCOL drive cycle, which showed the strategy adaptability;
3) The numerical results for the HWYCOL drive cycle showed that the phase-lag compensator can restore the UC terminal voltage without affect its power deliver in high power demands when compared to the PI and LPF strategies by relaxing the voltage restoration.
4) Although the IAE is the largest with the PLC, the LIB power dynamic is not highly affected by the UC voltage restoration. This is verified by the lowest wavelet detail coefficient standard deviation and the highest final SoH, indicating a lifetime 2.74% and 10.96% increased compared to traditional PI and LPF methods, respectively;
5) The experimental results demonstrated a 18.28% and 47.54% lower total operational cost compared to XOS and IT2-FLC strategies adapted from the literature. Moreover, for the SC03 drive cycle, the Haar Wavelet decomposition indicates a lower LIB stress with the proposed strategy and a LIB lifetime about 1.67 and 2.45 times higher than the XOS and IT2-FLC strategies, respectively, according the final SoH;

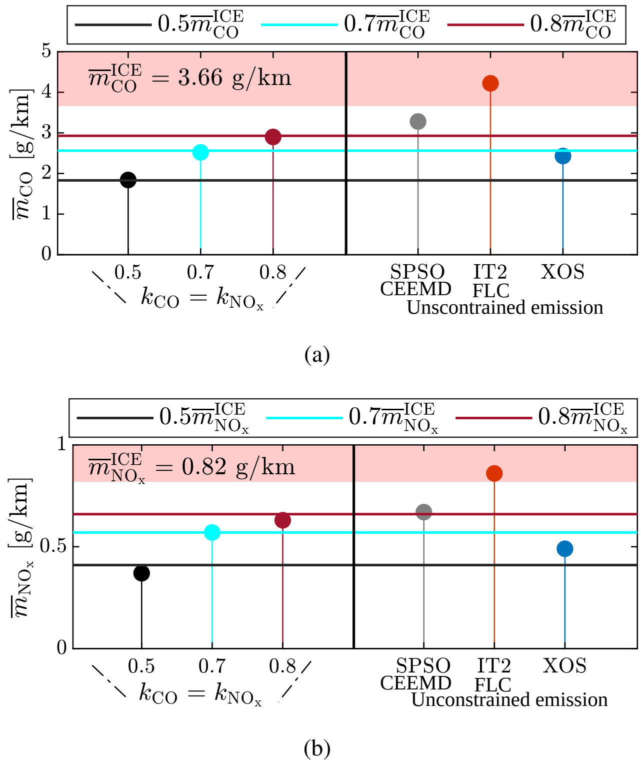

FIGURE 22. Average emissions under the unconstrained optimization and the constrained optimization for different values of k_{CO} and $k_{\mathrm{NO_x}}$: (a) CO emission and (b) $\mathrm{NO_x}$ emission.

6) Considering the emission constraints in the optimization problem, the experimental results indicate that emissions can be reduced depending on the optimization parameter selection. However, emission reduction leads to increased LIB usage, as reflected in the final SoH analysis, where the LIB lifetime is extended by a factor of 1.44 when emission constraints are not considered.

The simplicity and efficacy of the proposed SPSO-CEEMD strategy position it as a promising benchmark for EMSs. Future work includes incorporating the ICE gas emissions pricing according the carbon credit in the optimization and enhancing the proposed strategy by integrating driving speed prediction, enabling real-time optimization.

REFERENCES

[1] G. P. Incremona and P. Polterauer, "Design of a switching nonlinear mpc for emission aware ecodriving," IEEE Transactions on Intelligent Vehicles, vol. 8, DOI 10.1109/TIV.2022.3140484, no. 1, pp. 469–480, 2023.

[2] X. Sun, Z. Jin, M. Xue, and X. Tian, "Adaptive ECMS with gear shift control by grey wolf optimization algorithm and neural network for plug-in hybrid electric buses," IEEE Transactions on Industrial Electronics, vol. 71, DOI 10.1109/TIE.2023.3243304, no. 1, pp. 667–677, 2024.

[3] Y. Shen, J. Xie, T. He, L. Yao, and Y. Xiao, "CEEMD-fuzzy control energy management of hybrid energy storage systems in electric vehicles," IEEE Transactions on Energy Conversion, vol. 39, DOI 10.1109/TEC.2023.3306804, no. 1, pp. 555–566, 2024.

[4] M. V. R. Campos, L. J. R. Silva, T. A. Fagundes, R. V. A. Neves, V. A. Oliveira, and R. Q. Machado, "Energy management system based on s-shaped functions for series hybrid vehicle under a fully active topology," IEEE Transactions on Vehicular Technology, DOI 10.1109/TVT.2024.3498703, pp. 1–16, 2024.

[5] N. Yang, L. Han, R. Liu, Z. Wei, H. Liu, and C. Xiang, "Multi-objective intelligent energy management for hybrid electric vehicles based on multiagent reinforcement learning," IEEE Transactions on Transportation Electrification, vol. 9, DOI 10.1109/TTE.2023.3236324, no. 3, pp. 4294–4305, 2023.

[6] J. L. Wert, F. Safdarian, D. Wallison, J. K. Jung, Y. Liu, T. J. Overbye, and Y. Xu, "Spatiotemporal operational emissions associated with light-, medium-, and heavy-duty transportation electrification," IEEE Transactions on Transportation Electrification, vol. 10, DOI 10.1109/TTE.2023.3275050, no. 1, pp. 859–874, 2024.

[7] A. K. Podder, O. Chakraborty, S. Islam, N. Manoj Kumar, and H. H. Alhelou, "Control strategies of different hybrid energy storage systems for electric vehicles applications," IEEE Access, vol. 9, DOI 10.1109/ACCESS.2021.3069593, pp. 51 865–51 895, 2021.

[8] Z. Zhou, B. Duan, Y. Kang, Q. Zhang, Y. Shang, and C. Zhang, "Online state of health estimation for series-connected LiFePO4 battery pack based on differential voltage and inconsistency analysis," IEEE Transactions on Transportation Electrification, vol. 10, no. 1, pp. 989–998, 2023.

[9] L. Timilsina, P. R. Badr, P. H. Hoang, G. Ozkan, B. Papari, and C. S. Edrington, "Battery degradation in electric and hybrid electric vehicles: A survey study," IEEE Access, vol. 11, pp. 42 431–42 462, 2023.

[10] M. O. Badawy, M. Sharma, C. Hernandez, A. Elrayyah, S. Guerra, and J. Coe, "Model predictive control for multi-port modular multilevel converters in electric vehicles enabling hesds," IEEE Transactions on Energy Conversion, vol. 37, no. 1, pp. 10–23, 2021.

[11] X. Tang, J. Chen, T. Liu, Y. Qin, and D. Cao, "Distributed deep reinforcement learning-based energy and emission management strategy for hybrid electric vehicles," IEEE Transactions on Vehicular Technology, vol. 70, DOI 10.1109/TVT.2021.3107734, no. 10, pp. 9922–9934, 2021.

[12] M. Zha, W. Wang, C. Yang, X. Du, R. Chen, Y. Wang, and J. Su, "Time-efficient battery temperature sensitive energy management strategy for series hybrid electric vehicle," IEEE Transactions on Vehicular Technology, vol. 73, DOI 10.1109/TVT.2024.3406834, no. 10, pp. 14 689–14 703, 2024.

[13] X. Tang, J. Chen, H. Pu, T. Liu, and A. Khajepour, "Double deep reinforcement learning-based energy management for a parallel hybrid electric vehicle with engine startstop strategy," IEEE Transactions on Transportation Electrification, vol. 8, DOI 10.1109/TTE.2021.3101470, no. 1, pp. 1376–1388, 2022.

[14] B. Hu, B. Liu, and S. Zhang, "A data-driven reinforcement learning based energy management strategy via bridging offline initialization and online fine-tuning for a hybrid electric vehicle," IEEE Transactions on Industrial Electronics, vol. 71, DOI 10.1109/TIE.2024.3357870, no. 10, pp. 12 869–12 878, 2024.

[15] D. Phan, A. Bab-Hadiashar, M. Fayyazi, R. Hoseinnezhad, R. N. Jazar, and H. Khayyam, "Interval type 2 fuzzy logic control for energy management of hybrid electric autonomous vehicles," IEEE Transactions on Intelligent vehicles, vol. 6, no. 2, pp. 210–220, 2020.

[16] W. Shabbir and S. A. Evangelou, "Exclusive operation strategy for the supervisory control of series hybrid electric vehicles," IEEE Transactions on Control Systems Technology, vol. 24, no. 6, pp. 2190–2198, 2016.

[17] B. Chen, X. Pan, and S. A. Evangelou, "Optimal energy management of series hybrid electric vehicles with engine start–stop system," IEEE Transactions on Control Systems Technology, vol. 31, no. 2, pp. 660–675, 2022.

[18] G. Pease, D. Limebeer, and P. Fussey, "Fuel consumption minimization, with emissions constraints, for diesel powered cars," IEEE Transactions on Control Systems Technology, vol. 28, DOI 10.1109/TCST.2019.2908936, no. 4, pp. 1243–1257, 2020.

[19] W. Hong, I. Chakraborty, H. Wang, and G. Tao, "Co-optimization scheme for the powertrain and exhaust emission control system of hybrid electric vehicles using future speed prediction," IEEE Transactions on Intelligent Vehicles, vol. 6, DOI 10.1109/TIV.2021.3049296, no. 3, pp. 533–545, 2021.

[20] A. Benmouna, M. Becherif, L. Boulon, C. Dépature, and H. S. Ramadan, "Efficient experimental energy management operating for fc/battery/sc vehicles via hybrid artificial neural networks-passivity based control," Renewable Energy, vol. 178, pp. 1291–1302, 2021.

[21] D. Tang and H. Wang, "Energy management strategies for hybrid power systems considering dynamic characteristics of power sources," IEEE Access, vol. 9, pp. 158 796–158 807, 2021.

[22] Q. Lu, W. Zhou, and Y. Zheng, "Regenerative braking control strategy with real-time wavelet transform for composite energy buses," Machines, vol. 10, no. 8, p. 673, 2022.

[23] Y. Shen, S. Sun, Y. Li, W. Liang, X. Zhang, and X. Yuan, "Closed-loop haar wavelet power splitting method for vehicle-mounted hybrid energy storage system," IEEJ Transactions on Electrical and Electronic Engineering, vol. 18, no. 2, pp. 235–242, 2023.

[24] J. Wang, C. Du, F. Yan, X. Duan, M. Hua, H. Xu, and Q. Zhou, "Energy management of a plug-in hybrid electric vehicle using bayesian optimization and soft actor-critic algorithm," IEEE Transactions on Transportation Electrification, DOI 10.1109/TTE.2024.3398046, pp. 1–1, 2024.

[25] F. Tao, L. Zhu, Z. Fu, P. Si, and L. Sun, "Frequency decoupling-based energy management strategy for fuel cell/battery/ultracapacitor hybrid vehicle using fuzzy control method," IEEE Access, vol. 8, pp. 166 491–166 502, 2020.

[26] Z. Fu, L. Zhu, F. Tao, P. Si, and L. Sun, "Optimization based energy management strategy for fuel cell/battery/ultracapacitor hybrid vehicle considering fuel economy and fuel cell lifespan," International Journal of Hydrogen Energy, vol. 45, no. 15, pp. 8875–8886, 2020.

[27] K. Yang, X. Tang, S. Qiu, S. Jin, Z. Wei, and H. Wang, "Towards robust decision-making for autonomous driving on highway," IEEE Transactions on Vehicular Technology, vol. 72, DOI 10.1109/TVT.2023.3268500, no. 9, pp. 11 251–11 263, 2023.

[28] N. E. Huang, Z. Shen, S. R. Long, M. C. Wu, H. H. Shih, Q. Zheng, N.-C. Yen, C. C. Tung, and H. H. Liu, "The empirical mode decomposition and the hilbert spectrum for nonlinear and non-stationary time series analysis," Proceedings of the Royal Society of London. Series A: mathematical, physical and engineering sciences, vol. 454, no. 1971, pp. 903–995, 1998.

[29] Z. Zhang and W.-C. Hong, "Electric load forecasting by complete ensemble empirical mode decomposition adaptive noise and support vector regression with quantum-based dragonfly algorithm," Nonlinear dynamics, vol. 98, no. 2, pp. 1107–1136, 2019.

[30] J. Han, A. Khalatbarisoltani, Y. Yang, and X. Hu, "Energy management in plug-in hybrid electric vehicles: Preheating the battery packs in low-temperature driving scenarios," IEEE Transactions on Intelligent Transportation Systems, vol. 25, DOI 10.1109/TITS.2023.3317637, no. 2, pp. 1978–1991, 2024.

[31] R. F. Bastos, C. R. Aguiar, A. Balogh, Z. Sütő, and R. Q. Machado, "Power-sharing for dc microgrid with composite storage devices and voltage restoration without communication," International Journal of Electrical Power & Energy Systems, vol. 138, p. 107928, 2022.

[32] C. Arunkumar and U. B. Manthati, "A hybrid controller assisted voltage regulation and power splitting strategy for battery/supercapacitor system in isolated dc microgrid," IEEE Transactions on Energy Conversion, vol. 38, no. 3, pp. 1544–1553, 2023.

[33] L. J. R. Silva, M. V. R. Campos, B. M. Zilli, T. A. Fagundes, R. V. A. Neves, R. Q. Machado, and V. A. Oliveira, "A sigmoid-weighted-consensus for balancing multiple battery energy storage systems," IEEE Transactions on Industrial Electronics, DOI 10.1109/TIE.2024.3443958, pp. 1–11, 2024.

[34] T. A. Fagundes, G. H. F. Fuzato, R. F. Q. Magossi, L. J. R. Silva, J. C. Vasquez, J. M. Guerrero, and R. Q. Machado, "A modified redundancy-based energy management system for microgrids: An soc enhancement approach," IEEE Transactions on Industrial Electronics, vol. 71, DOI 10.1109/TIE.2023.3342325, no. 10, pp. 12 379–12 388, 2024.

[35] J. Wu, Z. Wei, W. Li, Y. Wang, Y. Li, and D. U. Sauer, "Battery thermal-and health-constrained energy management for hybrid electric bus based on soft actor-critic drl algorithm," IEEE Transactions on Industrial Informatics, vol. 17, no. 6, pp. 3751–3761, 2020.

[36] J. Xue and X. Jiao, "Speed cascade adaptive control for hybrid electric vehicle using electronic throttle control during car-following process," ISA transactions, vol. 110, pp. 328–343, 2021.

[37] H. Peng, T. Wu, L. Shen, and X. Miao, "Experimental investigations on control strategy of regulated two-stage turbocharging system for diesel engine under transient process," IEEE Access, vol. 10, pp. 104 461–104 471, 2022.

[38] R. Song, X. Liu, Z. Wei, F. Pan, Y. Wang, and H. He, "Safety and longevity-enhanced energy management of fuel cell hybrid electric vehicle with machine learning approach," IEEE Transactions on Transportation Electrification, vol. 10, DOI 10.1109/TTE.2023.3295433, no. 2, pp. 2562–2571, 2024.

[39] M. H. Miranda, F. L. Silva, M. A. Lourenço, J. J. Eckert, and L. C. Silva, "Electric vehicle powertrain and fuzzy controller optimization using a planar dynamics simulation based on a real-world driving cycle," Energy, vol. 238, p. 121979, 2022.

[40] J. P. Pauwelussen, Essentials of vehicle dynamics. Butterworth-Heinemann, 2014.

[41] A. Rohan, F. Asghar, and S. H. Kim, "Design of fuzzy logic tuned pid controller for electric vehicle based on ipmsm using flux-weakening," Journal of Electrical Engineering and Technology, vol. 13, no. 1, pp. 451–459, 2018.

[42] B. C. Ribeiro, A. L. P. de Oliveira, I. S. M. Luna, S. T. C. A. dos Santos, and J. R. B. de Almeida Monteiro, "Electric vehicle dynamics emulation with pmsm sensorless vector control," in 2023 15th IEEE International Conference on Industry Applications (INDUSCON), pp. 478–484. IEEE, 2023.

[43] T. A. Fagundes, G. H. F. Fuzato, L. J. R. Silva, A. M. d. S. Alonso, J. C. Vasquez, J. M. Guerrero, and R. Q. Machado, "Battery energy storage systems in microgrids: A review of soc balancing and perspectives," IEEE Open Journal of the Industrial Electronics Society, DOI 10.1109/OJIES.2024.3455239, pp. 1–32, 2024.

[44] D. Szpica, "New leiderman–khlystov coefficients for estimating engine full load characteristics and performance," Chinese Journal of Mechanical Engineering, vol. 32, no. 1, p. 95, 2019.

[45] J. S. Fabila-Carrasco, C. Tan, and J. Escudero, "Permutation entropy for graph signals," IEEE Transactions on Signal and Information Processing over Networks, vol. 8, pp. 288–300, 2022.

[46] S. Grassi, H. Huang, L. Pareschi, and J. Qiu, "Mean-field particle swarm optimization," in Modeling and Simulation for Collective Dynamics, pp. 127–193. World Scientific, 2023.

[47] G. Zhang, Q. Li, W. Chen, X. Meng, and H. Deng, "A coupled power-voltage equilibrium strategy based on droop control for fuel cell/battery/supercapacitor hybrid tramway," International Journal of Hydrogen Energy, vol. 44, no. 35, pp. 19 370–19 383, 2019.

[48] Q. Xun, N. Murgovski, and Y. Liu, "Joint component sizing and energy management for fuel cell hybrid electric trucks," IEEE Transactions on Vehicular Technology, vol. 71, no. 5, pp. 4863–4878, 2022.

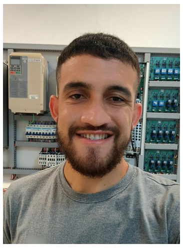

LUCAS JONYS RIBEIRO SILVA (Graduate Student Member, IEEE) was born in Viçosa, Brazil, in 1997. He received the B.S. in electrical engineering in 2020 from The Federal University of Viçosa and the M.S. degree in 2022 from the University of Sao Paulo. He is currently working on his Ph.D. in electrical engineering at the University of Sao Paulo. His main research interest are in the fields of microgrids, electric and hybrid vehicles, energy management and dc/dc converters for renewable energy sources and storage systems.

MÁRCIO VON RONDOW CAMPOS was born in Caratinga, Brazil, in 1996. He received the B.S in electrical engineering in 2022 from the Federal University of Viçosa. He is currently working on his M.S in electrical engineering at the University of Sao Paulo and his mains research interest are in the fields of dc/dc converters for renewable energy sources, microgrids, energy management and hybrid or pure electric vehicles.

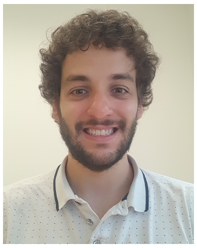

THALES AUGUSTO FAGUNDES received the B.S. in electrical engineering in 2017 and the M.S. degree in 2020 from the University of Sao Paulo. In 2014, he studied abroad at the University of New South Wales, Australia. He is currently working on his Ph.D. in electrical engineering at the University of Sao Paulo and from 2022 to 2023 he was a visiting researcher at the Aalborg University. His main research interest are in the fields of microgrids, energy management and DC-DC converters for renewable energy sources and storage systems.

BRUNO MENEGHEL ZILLI received the B.S. in electronic engineering in 2015 from the Federal University of Technology-Paraná and the M.S. degree in Energy in Agriculture Engineering from the Western Paraná State University, 2018. He is currently working on his Ph.D. in electrical engineering at the University of Sao Paulo. His main research interest are in the fields of microgrids, harmonic compensation, energy management and renewable energy sources.

RODOLPHO VILELA ALVES NEVES received the B. S. from the Federal University of Viçosa (UFV), Brazil, in 2011, and the M.Sc. and D.Sc. in Electrical Engineering from the University of Sao Paulo, Sao Carlos, Brazil, in 2013 and 2018, respectively. From 2015 to 2016, he was a Visiting Researcher at Aalborg University, Denmark. He is currently an Adjunct Professor in the Department of Electrical Engineering at UFV. His research interests include intelligent control strategies and modeling dynamic systems.

RICARDO QUADROS MACHADO (Senior Member, IEEE) received the B. S. from the University of Santa Maria in 1997, the M.S. (2000) and the Ph.D. (2005) degrees in Electrical Engineering from the University of Campinas. From 2002 to 2003 he was a visiting researcher at the University of Padova, Italy and from 2005 to 2007 he was a post-doctorate at the Federal University of Santa Maria, Brazil. From 2013 to 2014 he was visiting professor at the University of Toronto, Canada. Currently, he is associated professor at the University of Sao Paulo and his main research interests are: processing of energy in dc/dc and dc/ac converters, digital control of power converters, distributed generation systems, smart grids and control of renewable energy sources.

VILMA ALVES DE OLIVEIRA (Life Senior Member, IEEE) received the B.Eng. degree in electronics from the Rio de Janeiro State University, Rio de Janeiro, Brazil, in 1976, the M.Sc. degree from the Federal University of Rio de Janeiro, Rio de Janeiro, in 1980, and the Ph.D. degree from the University of Southampton, Southampton, U.K., in 1989, both in electrical engineering. In 1990, she joined the Department of Electrical and Computing Engineering, University of Sao Paulo, Sao Paulo, Brazil, where she is currently a Full Professor. Her research interests include fuzzy control and control design and its applications. Prof. Oliveira is currently the Editor in Chief for the Journal of Control, Automation and Electrical Systems.